ORIGINAL ARTICLE

Vadose Zone Journal [OPEN ACCESS]

Spatial variability of hydraulic parameters of a cropped soil using horizontal crosshole ground penetrating radar

Lena Lärm [ID] | **Lutz Weihermüller** [ID] | **Jan Rödder** | **Jan van der Kruk** [ID] |
Harry Vereecken [ID] | **Anja Klotzsche** [ID]

Agrosphere (IBG-3), Institute of Bio- and Geosciences, Forschungszentrum Jülich, Jülich, Germany

Correspondence
Lena Lärm, Agrosphere (IBG-3), Institute of Bio- and Geosciences, Forschungszentrum Jülich, Jülich, Germany.
Email: l.laerm@fz-juelich.de

Assigned to Associate Editor Zhuanfang Zhang.

Abstract

Soil hydraulic parameters (SHP) play a crucial role controlling the spatiotemporal distribution of water in the soil–plant continuum and thus affect water availability for crops. To provide reliable information on the SHP at different scales, measurement techniques with a good spatial resolution and low labor costs are required. In this study, we used crosshole ground penetrating radar (GPR)-derived soil water contents (SWCs) measured along horizontal rhizotubes under a controlled experimental test site cropped with winter wheat to estimate the unimodal and dual-porosity soil hydraulic characteristics with different soil layer setups. Therefore, sequential inversion of the GPR-derived SWCs was performed using the hydrological model HYDRUS-1D, whereby the SWC data were either averaged prior inversion or used in a spatially distributed way. To analyze if the time-lapse gathered GPR data contain enough information to estimate the SHP, additional synthetic studies were performed increasing the data resolution to daily GPR measurements. The results showed that the time-lapse data contained enough information to estimate the SHP accurately. Additionally, spatially distributed soil hydraulic characteristics differed from the one estimated based on averaged SWCs derived from spatially distributed GPR data. Finally, we derived spatially resolved SHP, which can be used for 3D process rhizosphere processes and root–soil interaction modeling.

Plain Language Summary

This study explores the use of ground penetrating radar (GPR) to estimate soil hydraulic parameters (SHP), which are crucial for understanding water distribution in soil and its availability to crops. GPR is used to measure soil water content along

Abbreviations: AICc, corrected Akaike Information Criteria; EMI, electromagnetic induction; ERT, electrical resistivity tomography; FC, field capacity; GPR, ground penetrating radar; HCC, hydraulic conductivity characteristics; LAI, leaf area index; MR, minirhizotron; PAW, plant available water; PWP, permanent wilting point; RMSE, root mean square error; SHP, soil hydraulic parameters; SSR, sum of squared residuals; SWC, soil water content; SWR, soil water retention; ZOP, zero-offset-profiling.

horizontal tubes in a winter wheat field. They then used these data to estimate soil hydraulic characteristics using different soil layer and hydraulics setups. The key findings were: inverting time-lapse GPR data can estimate SHP, the method allowed for the derivation of spatially resolved SHP, and spatially distributed soil hydraulic characteristics differed from those estimated using averaged soil water content. These findings suggest that GPR can be an effective tool for measuring SHP with good spatial resolution and lower labor costs. The resulting spatially resolved parameters can be valuable for modeling 3D rhizosphere processes and root–soil interactions, potentially improving our understanding of crop water availability and management.

1 | INTRODUCTION

Understanding the hydraulic processes within the vadose zone is important for various applications including environmental studies, ecosystem science, agriculture, soil science, meteorology, and hydrology. To investigate the wide range of processes that influence the hydrological response between the subsurface and the atmosphere, it is necessary to observe the hydrological systems at different scales (Vereecken et al., 2008, 2022). For example, small-scale modeling of rhizosphere processes and root–soil interactions requires information on the processes and parameters at the point- to rhizosphere(pedon)-scale (Schnepf et al., 2022), whereas Land-surface or Earth system models used for ecosystem quantification and prediction require information at the field to regional scale (Looy et al., 2017; Simmer et al., 2015; Vereecken et al., 2016). To supply the models with appropriate input, methods are therefore needed to provide soil parameters at different scales. When hydrological dynamics are of primary concern, the soil water retention (SWR) and hydraulic conductivity characteristics (HCC) must be known, whereby the soil hydraulic parameters (SHP) are conventionally derived either directly or indirectly. Direct methods are mainly based on laboratory experiments, which are costly and labor intensive (Durner & Lipsius, 2005). In general, laboratory measurements of hydrological dynamics (SWR and HCC) are based on a variety of techniques using small-scale soil columns of a few cm^3 (typically 100–300 cm^3) in volume. In the field, SHP can also be estimated by the use of in situ soil sensors such as matric potential and SWC sensors, but this approach is limited by the small sensing volume of those sensors and the transferability of the results to the pedon scale, as at the pedon scale a different representative elementary volume might be present compared to those measured by the small-scale sensors. To acquire information on a plot to field scale, it is common practice to repeat the small-scale point measurements (usually by taking undistorted samples for laboratory measurements) for several locations and to upscale the laboratory hydraulic parameters to the entire field site. The

same might hold for the use of soil sensors used, for example, in sensor networks (e.g., Bogena et al., 2007). Although, a detailed vertical representation of the heterogeneous soil can be mapped at the point locations (often done during sampling or sensor installation), spatial distributions (laterally) between the points and small-scale heterogeneities cannot be captured (Kool et al., 1987).

Alternatively, geophysical methods have been widely used to estimate SWCs at the field to plot scale and the SHP have been estimated from those measurements over the last two decades to fill the gap between point and plot to field scale. Most popular geophysical techniques are electrical resistivity tomography (ERT) (Brunet et al., 2010; Jayawickreme et al., 2010; Michot et al., 2003; Samouëlian et al., 2005), electromagnetic induction (EMI) (Altdorff et al., 2017; Brosten et al., 2011; Corwin & Lesch, 2005; Doolittle & Brevik, 2014; Moghadas et al., 2017; Sheets & Hendrickx, 1995), and ground penetrating radar (GPR) (Huisman et al., 2003; Klotzsche et al., 2018). While ERT and EMI provide the electrical conductivity as physical quantity, GPR is able to provide both the dielectric permittivity and electrical conductivity. Using petrophysical relationships such as Archie's law (Archie, 1942) for electrical conductivity or Topp's equation for dielectric permittivity (Topp et al., 1980), both properties can be related to soil water content (SWC).

Time-lapse geophysical datasets combined with sequential or coupled inversion approaches can be used as inputs to estimate the soil hydraulic characteristics (SWR and HCC). For the sequential inversion, the geophysical quantity such as electrical conductivity or GPR travel time (related to relative dielectric permittivity) is first converted to SWC. In the second step, these derived SWCs estimates are used in an inversion to estimate the SHP using appropriate hydrological models. This approach has been successfully applied to obtain the SHP from ERT (Beaujean et al., 2014; Camporese et al., 2015; Claes et al., 2020; Huisman et al., 2010; Manoli et al., 2015; Pleasants et al., 2022, 2023). Other successful studies have been performed with surface (Busch et al., 2013) and crosshole GPR (Looms et al., 2008;

Rucker & Ferré, 2004; Yu et al., 2021). The term "sequential inversion" as used by Yu et al. (2021) is not consistently used in the literature. For example, Yeh and Šimůnek (2002) used the term *Level 1 data fusion*, Doetsch et al. (2012), Farmani et al. (2008), and Kemna et al. (2002) used no specific term for their inversion approach, whereas Beaujean et al. (2014), Camporese et al. (2015), Claes et al. (2020), González-Quirós and Comte (2021), Hinnell et al. (2010), Irving and Singha (2010), and Pleasants et al. (2022, 2023) used the term *uncoupled hydrogeophysical inversion* to describe the same inversion approach. As the data are inverted sequentially (e.g., geophysical signal to SWC first and those SWC to soil hydraulic parameter second), we prefer the use of the term sequential inversion.

A more complex inversion scheme is the coupled hydrogeophysical inversion, where the geophysical information is not converted to SWC prior to the inversion but used directly as information in the geophysical inversion process (Hinnell et al., 2010). In general, the coupled inversion can overcome potential errors introduced by the geophysical inversion, and, therefore, this inversion scheme can be more reliable. On the other hand, any error introduced by the choice of the petrophysical transformation (e.g., from SWC to dielectrical permittivity) will be still existing in the coupled inversion approach. Additionally, any shortcomings in the hydrological model, such as wrong process representation, will also propagate into the results of the coupled inversion. Finally, as some coupled inversion schemes require state-of-the-art hydrological and geophysical models, both of which are often computationally demanding, the computational requirements are increased in contrast to the sequential inversion approach (Yu et al., 2021). Coupled inversions have been performed by Mboh et al. (2011), Kuhl et al. (2018), and Tran et al. (2016) for ERT and by Yu et al. (2021) for GPR. Yu et al. (2021) compared the performance and the reliability of both inversion approaches for GPR data acquired during an infiltration experiment. It was observed that in the presence of fast dynamics caused by infiltration or heavy rainfall, a coupled inversion should be considered, while for long-term investigations covering entire seasons, a sequential inversion can be equally efficient.

Even though most geophysical techniques can determine the SWC in either two dimensions (Cassiani et al., 2012; Klotzsche et al., 2019; Lärm et al., 2024) or even three-dimensions (Beff et al., 2012; Koestel et al., 2008), the SHP were primarily estimated in one dimension (e.g., Busch et al., 2013; Jadoon et al., 2012). To our knowledge, a two- or three-dimensional estimation of the soil hydraulic characteristics (SWR and HCC), or more precisely of the horizontal spatially distributed SHP describing the soil hydraulic characteristics for multiple soil layers at high resolution of only a few centimeters, based on geophysical field data, has yet not been performed.

Core Ideas

- 1D and semi-3D soil hydraulic parameters from ground penetrating radar (GPR) using sequential inversion were derived.
- The GPR-derived soil water contents with a hydrological model were combined.
- Parameters for crop growth studies and their spatial variability were obtained.

Especially, for small-scale field trials such as those used in breeding and fertilization experiments, the small-scale heterogeneity of the underlying soil might be significant for both analysis and the modeling processes involved in crop growth (Lynch, 2007). Hereby, it is established that water and nutrient uptake by the plants through their root system is heavily reliant on the current water and nutrient availability in the small-scale volume surrounding the roots (rhizosphere), where even small changes can significantly affect the crop performance (Bauke et al., 2022; Landl et al., 2019; Schnepf et al., 2022). In addition, biochemical processes like greenhouse gas (GHG) formation often depend on the conditions of designated hotspots (e.g., Kravchenko et al., 2017). Therefore, the knowledge of the two- or three-dimensional states of the soil (e.g., water content and matric potential) is important, and these information can generally be predicted by spatially resolved models. Additionally, the estimated SHP can be used to derive secondary soil characteristics, such as field capacity (FC), permanent wilting point (PWP), and plant available water (PAW). PAW describes potential availability of water in the root zone for transpiration, and, hence, is an important parameter to describe crop growth and productivity of both rain-fed and irrigated crops. PAW can also be used to estimate irrigation needs during drought periods, and, therefore, can help in decreasing water and energy consumption required for irrigation and be beneficial to inform soil water management decisions (Amsili et al., 2024; Poggio et al., 2010). In comparison to mean field information of the soil hydraulic characteristics, the spatial knowledge can be also beneficial to inform three-dimensional agroecosystem models across different scales as stated by Vereecken et al. (2022) and Vanderborght et al. (2023).

The objective of this study was to estimate the semi-3D representation of the SHP, which is derived from horizontal one-dimensional GPR-derived SWC planes measured within horizontal boreholes (rhizotubes) across various depth within a minirhizotron (MR) facility. Therefore, soil characteristics across a controlled experimental test site cropped with winter wheat, providing detailed information about a soil volume with the dimensions 3.0 by 0.75 by 1.2 m (length, width, and depth). To achieve this, we utilized a sequential
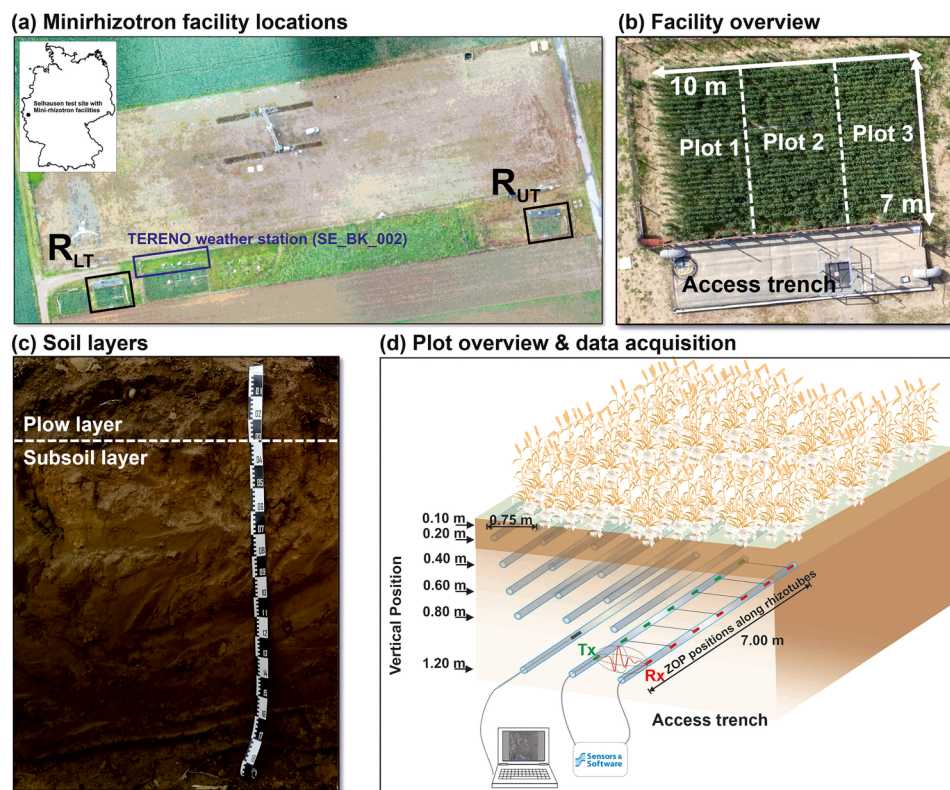
FIGURE 1 (a) Aerial overview of the minirhizotron (MR) facilities in Selhausen, Germany, and a map of the location in Germany. (b) Birds view of the plots and access trench. (c) Photo of the soil layers for the lower terrace (R_{LT}) MR facility and (d) schematic illustration of a plot within the minirhizotron facility and the zero-offset profiling ground penetrating radar (GPR) measurement and root imaging setup. Adapted from Lärm et al. (2024). TERENO, TERrestrial ENvironmental Observatories.

hydrogeophysical inversion and time-lapse horizontal cross-hole GPR-derived SWC measurements. The study was performed in two steps: first, the SWC gathered by GPR were horizontal averaged and inverted; second, the individual GPR derived SWCs along the rhizotubes ($N = 61$) were inverted and compared to the averaged one to analyze the potential of inverting spatially distributed SHP. Additionally, different synthetic studies were performed to analyze first whether the data density gathered by GPR is adequate to reliable estimate the SHP and second, whether the sequential inversion is applicable under natural boundary conditions and if a more demanding coupled inversion scheme might be necessary.

2 | MATERIALS AND METHODS

2.1 | Data acquired at the MR facility Selhausen

To parameterize the hydrological model for this study, a comprehensive and detailed dataset was required. Therefore, we used data measured at one MR facility as described by Lärm et al. (2023) at the Selhausen test site (Figure 1a) located within the TERENO (TERrestrial ENvironmen-

tal Observatories) Eifel-Lower Rhine observatory in North Rhine-Westphalia, Germany (Bogena et al., 2018; Pütz et al., 2016). At this site, two identically constructed MR facilities were present, situated within different river sediments of the Rur river catchment (Bogena et al., 2018; Brogi et al., 2019; Weihermüller et al., 2007). The river sediments resulted in contrasting soil conditions, where at the upper terrace (R_{UT}) MR facility was located in a gravely, partly stony, and silty sand with skeleton contents larger 50%, whereas the lower terrace (R_{LT}) MR facility was located in a silty, sandy, and slightly gravely (<5% in skeleton) loess developed from eolian deposits of the Pleistocene and characterized as a Cutanic Luvisol (Ruptic, Siltic) (Bauer et al., 2011) based on the World Reference Base for Soil Resources (IUSS Working Group WRB, 2007). For this study, data from the R_{LT} MR facility were used. The soil contained 17% clay, 70% silt, and 13% sand as reported by Weihermüller et al. (2007). The soil comprised two distinct layers, namely, the topsoil or plow layer that spans from 0 to 30 cm and the subsoil located below (Figure 1c). For further details regarding the construction and setup of the MR facilities, we refer to the works by Cai et al. (2016) and Lärm et al. (2023). The MR facility accommodated three different field plots (see Figure 1b) allowing different agricultural treatments. In the years studied here, plot

TABLE 1 Overview crop management and measurements for the crop growing season 2016.

Crop cultivar	Winter wheat (cv. Ambello)
Sowing date	October 26, 2015
Flowering date	June 3, 2016
Harvest date	July 26, 2016
GPR measurements	20 (from March 30 to August 8, 2016)
Root measurements	22 (from November 16, 2015, to July 22, 2016)
LAI measurements	20 (from December 17 to July 22, 2016)

Abbreviations: GPR, ground penetrating radar; LAI, leaf area index.

1 was used as a rain-out shelter to mimic dryer conditions, plot 2 was left under natural/rain-fed conditions, and plot 3 was irrigated. Our investigation aimed to observe the effects of natural conditions, and, therefore, we focused on the center plot 2 of the R_{LT} MR facility (Figure 1b). Within this plot, three sets of horizontal rhizotubes with six depths ranging between 0.1 and 1.2 m and a horizontal separation of 0.75 m between the rhizotubes were available for measurements (Figure 1d). The GPR and root image (see details below) measurements were performed in these rhizotubes, which can be accessed from a belowground access trench (Figure 1b). The GPR dielectric permittivity data gathered have been published as part of a data paper by Lärm et al. (2023).

The field dataset was acquired during the crop growing season 2016 under winter wheat (cultivar Ambello) cultivation (Table 1). Crop management including pest control and fertilization were performed in compliance with regional standards. The wheat was sown with a seeding density of 300–320 grains per m^2 at a row separation of 12 cm perpendicular to the direction of the rhizotubes. The climatic variables used were obtained from the TERENO weather station (SE_BK_002) located approximately 15 m away (Figure 1a). The climatic data were measured in 10-min intervals and the potential grass evapotranspiration (ET_0) was derived according to FAO Irrigation and drainage paper 56 (Allen et al., 1998) as daily values. Climatic data (precipitation and ET_0) were used for the forcing of the soil hydrological model. Details of the calculation and gap filling of the potential grass evapotranspiration are described by Graf et al. (2020) and Rahmati et al. (2020).

The maximum rooting depth for various measurement dates was determined from available total root length values obtained from root image data captured using an MR camera (Bartz Technology Corporation) inserted inside the rhizotubes. The images were analyzed using an automatic image analysis pipeline developed by Bauer et al. (2022). Additionally, the leaf area index (LAI) was regularly measured during the vegetation period using a plant canopy analyzer (LIA-220, LI-COR Inc.).

2.2 | GPR-derived SWCs

GPR data were obtained through crosshole zero-offset-profiling (ZOP), wherein the transmitting antenna (Tx) and the receiving antenna (Rx) were placed in adjacent rhizotubes at the same depth. The measurements were taken using a 200 MHz PulseEKKO System from Sensors & Software on 20 measurement days during the vegetation period of winter wheat (see Table 1). In the following, a short description of data gathering and processing is provided.

The antennae were moved in parallel along the length of neighboring rhizotube with a 0.05 m measurement spacing. The standardized processing of crosshole GPR-ZOP data involved three steps: (1) de-wow filtering, (2) time-zero correction, and (3) detection of the first arrival time/first break to estimate the travel time for each measurement point (for further details, refer to Klotzsche et al. [2019]). The velocity of the electromagnetic wave was determined by utilizing the known distance of 0.75 m between the rhizotubes along with the estimated travel time from each ZOP measurement location. The calculated EM wave velocity, v, was converted into relative dielectric permittivity ε_r (-) using

$$\varepsilon_r = \left(\frac{c}{v}\right)^2, \tag{1}$$

where c indicates the speed of light (m s^{-1}). Considering appropriate petrophysical relationships or empirical equations, the volumetric SWC θ (cm^3 cm^{-3}) can be derived from the relative dielectric permittivity ε_r (Huisman et al., 2003; Steelman et al., 2011). According to Klotzsche et al. (2019), the GPR-derived SWC from the petrophysical relationships Complex Refractive Index Model (Roth et al., 1990) and Topp's equation (Topp et al., 1980) were similar for the soil, at the R_{LT}. Since Topp's equation does not require additional information on soil properties such as porosity, Topp's equation was finally used for the conversion of the dielectric permittivity to volumetric SWC.

$$\theta = -5.3 \times 10^{-2} + 2.92 \times 10^{-2}\varepsilon_r - 5.5 \times 10^{-4}\varepsilon_r^2$$
$$+ 4.3 \times 10^{-6}\varepsilon_r^3. \tag{2}$$

The GPR-derived SWC values at a depth of 0.1 m in the uppermost rhizotube produced unrealistically low SWC results due to interference from critically refracted air and direct waves (Klotzsche et al., 2016, 2019). Thus, these values were omitted from the study. Moreover, data gathered at either ends of the 7-m rhizotubes were excluded from the analysis, as they were affected by the access trench and soil sensors installed at one side of the facility and an excavation trench needed to install the rhizotron tubes at the other end of the MR facility. Consequently, only data within the range of 3–6 m from the access trench were included. This resulted in 61

GPR-derived SWC values for each depth measured between two rhizotubes installed per plot, which were combined to create a semi-3D horizontal SWC depth plane. Alternatively, one can use the mean SWC along each horizontal depth planes (each pair of rhizotubes), which seems reasonable for winter wheat because of its low crop row separation as suggested by Klotzsche et al. (2019). During the measurement season, a spectral electrical impedance tomography monitoring system as described by Weigand et al. (2022) was additionally installed between 5.5 and 6 m along the rhizotubes. Unfortunately, this system interferes with the measured GPR data, and, therefore, the data for this section within the depth of 0.2 m had to be disregarded as well.

2.3 | Soil hydrological modeling

The SHP were estimated from GPR-derived SWC using the HYDRUS-1D software (Šimůnek et al., 2013), which solves the one-dimensional Richards (1931) equation for a partially saturated, porous, and rigid medium:

$$\frac{\partial \theta (h)}{\partial t} = \frac{\partial}{\partial z} \left[K(h) \left(\frac{\partial h}{\partial z} \right) + 1 \right] - S, \tag{3}$$

where t is the time (days), z is the positive upward vertical coordinate (cm), and $K(h)$ is the unsaturated hydraulic conductivity (cm day^{-1}) as a function of the pressure head h (cm). For the atmospheric conditions, daily inputs of precipitation and potential grass evapotranspiration (ET$_0$) were used. The sink term S in Equation (3) determines the quantity of water extracted from the soil through root water uptake. To characterize root water uptake, we utilized the Feddes model (Feddes et al., 1974) and adapted the Feddes root water uptake parameters from Wesseling (1991) for wheat vegetation. Therefore, $P0$ was set to 0 cm, $P0_{opt}$ to -1 cm, $P2H$ to -5000 cm, $P2L$ to -9000 cm, and $P3$ to $-16,000$ cm. The simulation domain reached a depth of 200 cm and included the plow layer (0–30 cm) and a subsoil (Bt horizon) below. To better represent the site conditions in the hydraulic model, we tested a two- and three-layer model. For the three-layer model, we introduced a new soil layer between 100- and 200-cm depth. All models were discretized using 303 nodes, with the node spacing increasing with depth.

As the upper boundary condition, daily atmospheric conditions with surface runoff were used. Daily precipitation was distributed throughout the day using the sine function embedded in HYDRUS-1D. To differentiate potential transpiration $T0$ from ET$_0$ during crop growth, we utilized Beers Law:

$$T_0 = ET_0 \left(1 - e^{-k_r \times LAI} \right), \tag{4}$$

where k_r is the radiation extinction factor, which typically ranges between 0.5 and 0.75 (here set to 0.625). Since FAO 56 calculated ET$_0$ is only valid for a grass reference, the T_0 was adjusted during crop growth using K_c vales as a function of LAI with

$$T_0^{K_c} = T_0 \times K_c. \tag{5}$$

Thus, the crop coefficient (K_c) was set to 1 during the initial growth stages and increased to a maximum of 2 at maximum LAI during the flowering stage. K_c then decreased to 1.2 at harvest during the senescence period. The K_c values for intermediate periods were linearly interpolated as illustrated in Figure 2.

The allowable minimum pressure head at the soil surface (hCritA) was set at $-15,000$ cm, which results in a transition of the upper boundary from flux to a fixed pressure head. For the lower boundary, a predefined pressure head (cm), measured by tensiometers at a depth of 140 cm recorded close to the MR facility, was used. To calculate the pressure heads for the lower boundary of the simulation domain at 200 cm (total simulation depth), a constant offset of 60 cm was added to the values recorded at 140-cm depth assuming a linear decrease of matrix potential between 140- and 200-cm depth. Two functions were considered for describing the SWR and hydraulic conductivity curve. The first is the unimodal or single porosity Mualem–van-Genuchten (MvG) model (Mualem, 1976; van Genuchten, 1980), referred to hereafter as the unimodal model. The second is the bimodal or dual-porosity model introduced by Durner (1994), referred to hereafter as the dual-porosity model. In the case of a dual-porosity model, the SWR curve is described by:

$$\theta (h) = \theta_r + (\theta_s - \theta_r) \sum_{i=1}^{k} \omega_i Se_i \tag{6}$$

with

$$Se_i = \left[1 + |\alpha_i h|^{n_i} \right]^{-m_i}, \tag{7}$$

where θ_r and θ_s are the residual and the saturated water contents (cm^3 cm^{-3}), respectively, k is the order of porosity in the soil system (here $k = 1$ for the unimodal and $k = 2$ for dual-porosity model), Se is the effective saturation (-), ω_i is the weighting factor ($\sum \omega_i = 1$). α_i (cm^{-1}), n_i (-), and m_i (-) are the empirical parameters, whereby α_i can be related to the inverse of the air entry values and n_i to the width of the pore size distribution, whereas m_i is classically related to n_i by $m_i = 1 - 1/n_i$.

The relative soil hydraulic conductivity function $K(h)$ is given by Priesack and Durner (2006):

$$K(h) = K_s \sum_{i=1}^{k} \omega_i Se_i^{\lambda} \left[\frac{\sum_{i=1}^{k} \left(1 - \left(1 - Se_i^{1/m_i} \right) \right)^{m_i}}{\sum_{i=1}^{k} \omega_i \alpha_i} \right]^r \tag{8}$$
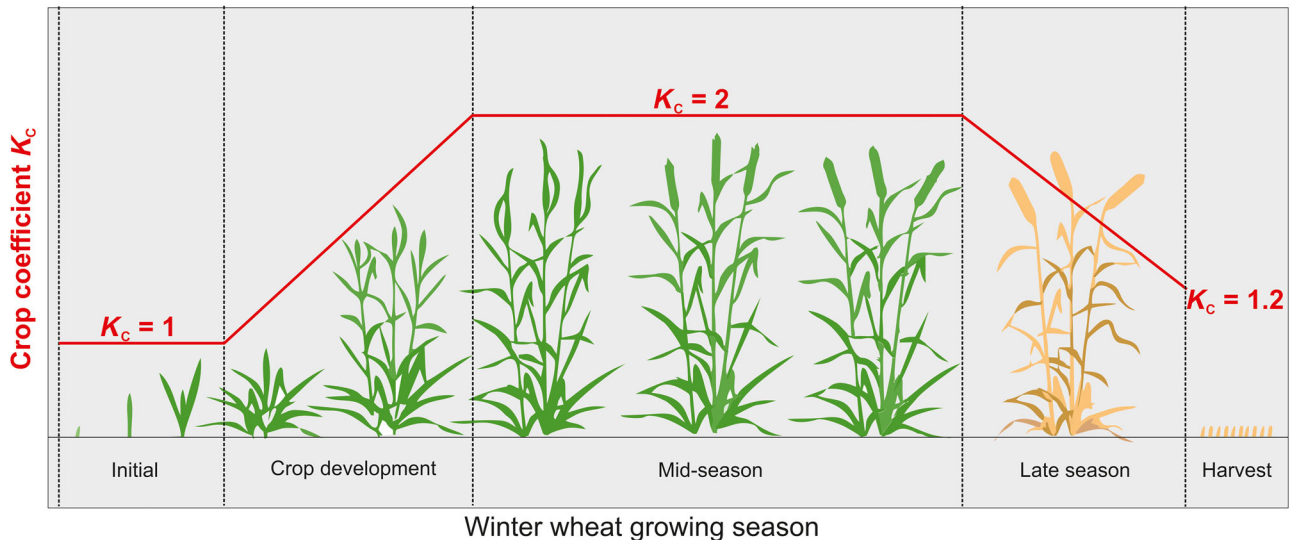
FIGURE 2 Crop coefficient K_c over the crop growing season of winter wheat. Adapated from Pokorny (2019).

where K_s (cm day^{-1}) is the saturated hydraulic conductivity, λ (-) is the tortuosity factor, and r is a shaping factor for the relative hydraulic conductivity function and set to $r = 2$ according to (Mualem, 1976). This dual-porosity model's parametrization assumes two components in the soil: (1) the soil matrix and (2) the macropores; unlike the unimodal model, which has only the matrix. As most crop growth models still need information on soil characteristics (FC, PWP, and PAW) to compute the water dynamics (Jarvis et al., 2022), the FC was calculated by determining the SWC at a pressure head of pF 1.8 (equivalent to a height of 330 cm), while PAW was calculated as the difference in SWC between FC and PWP, defined at a pressure head of pF 4.2 (equivalent to a height of 15,000 cm) (Novák & Hlaváčiková, 2018).

2.4 | Sequential inversion

To estimate the SHP of the MvG models (unimodal and dual-porosity model), the Shuffled-Complex-Evolution algorithm (SCE-UA) as described by Q. Y. Duan et al. (1993) and Q. Duan et al. (1994) was used. The SCE-UA is a global search routine that has been effectively utilized in hydrogeophysical inversion research conducted by Kuhl et al. (2018), Mboh et al. (2011), Busch et al. (2013), and Yu et al. (2021). The mismatch is calculated by using the squared sum of the differences between modeled SWC $\theta_{\text{mod}i,j}$ and observed SWC $\theta_{\text{obs}i,j}$ per depth in the corresponding layer N and for the corresponding measurement days (GPR$_{\text{days}}$). To normalize for the different height of the SWCs measured at different depth, the misfit was divided by the mean of the modeled SWC $\overline{\theta_{\text{mod}i}}$ per measurement depth N. Finally, the mismatch was further normalized by the number of measurement depths per layer to account for the different total number of measurements in each layer. Based on this, the cost function to be minimized

can be written as:

$$\text{CF} = \sum_{k=1}^{n_{\text{Layer}}} \frac{\sum_{i=1}^{N} \sum_{j=1}^{\text{GPR}_{\text{days}}} \left(\theta_{\text{mod}i,j} - \theta_{\text{obs}i,j} \right)^2}{\overline{\theta_{\text{mod}i}}} \times \frac{1}{N} \quad (9)$$

where CF is the normalized squared mean error, n_{Layer} is the number of modeled soil layers, θ_{obs} and θ_{mod} are the observed GPR-derived and HYDRUS-1D modeled SWC, respectively. The inversion was terminated, when the cost function did not improve more than 0.01% within the last 10 inversion loops. Except for λ, expert knowledge was utilized to choose the feasible space for the parameter optimization for all parameters. According to the study conducted by Peters et al. (2011), the lower boundary of the feasible space was set to $\lambda = -2$ to keep the hydraulic conductivity function monotonically decreasing. Finally, a model spin-up of 125 days was used to be independent on the initial conditions of the soil profile (see Figure 3a).

To find a hydrological model that best represents the water flux dynamics with respect to number of soil layers and soil hydraulic characteristics (unimodal vs. dual-porosity), four different model setups were tested, namely, a two-layered and a three-layered model with either unimodal or dual-porosity soil hydraulic characteristics. An overview of the averaged one-dimensional sequential inversion steps is shown in Figure 4a. Therefore, the determination of a most suitable model to describe the data is necessary. We utilized the corrected Akaike information criteria (AICc) (Burnham & Anderson, 2004):

$$\text{AICc} = N \ln \left(\frac{\text{SSR}}{N} \right) + 2n_{\text{SHP}} + \frac{2n_{\text{SHP}} \left(2n_{\text{SHP}} + 1 \right)}{N - n_{\text{SHP}} - 1}, \quad (10)$$
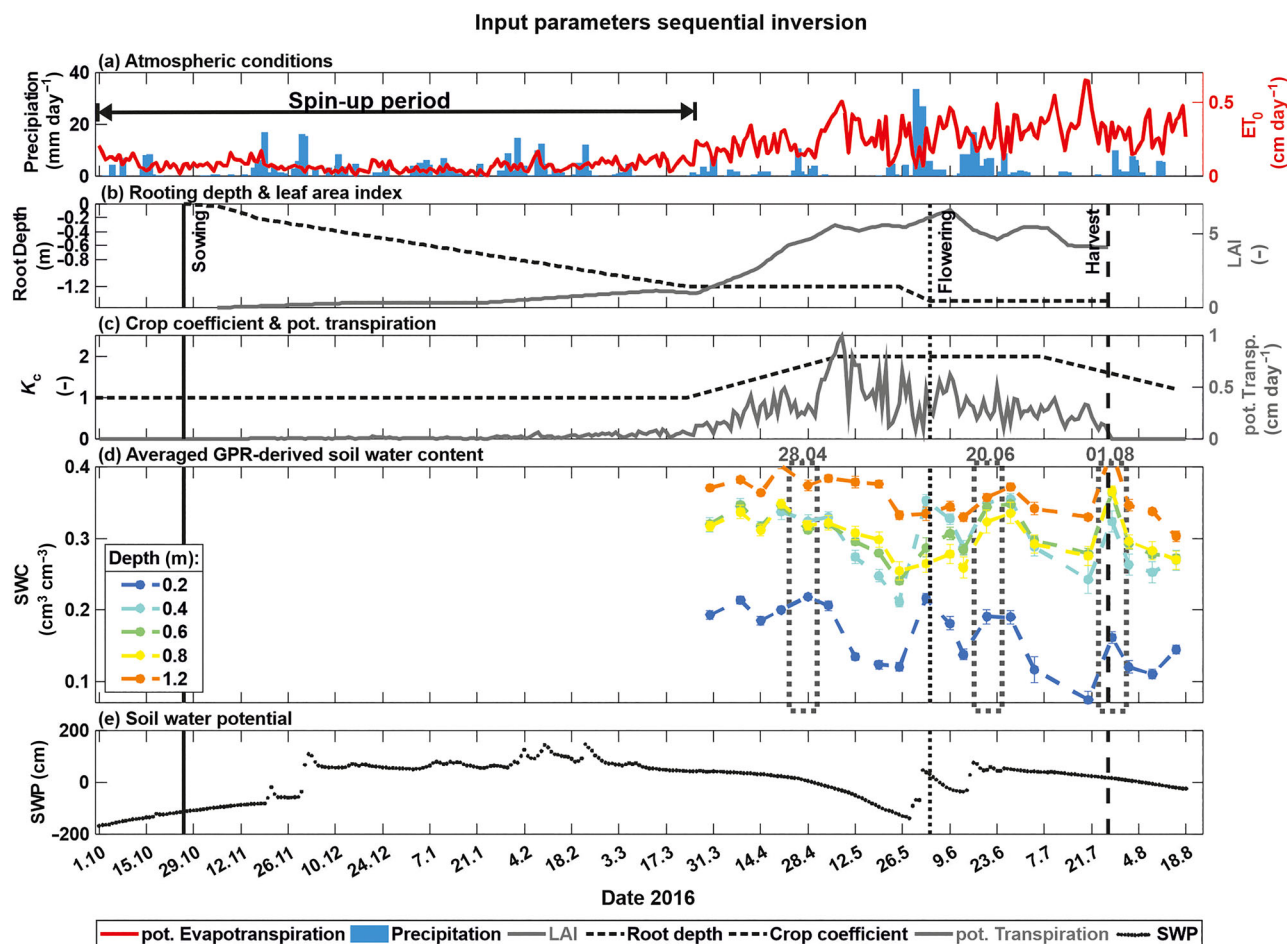
FIGURE 3 Parameters for the sequential inversion with (a) daily precipitation (blue bars), reference grass evapotranspiration (red line), and the black arrow indicates the spin-up period. (b) Leaf area index (LAI) (gray solid line) and the rooting depth (black dashed line). (c) Crop coefficient (black dashed line) and rescaled potential transpiration (gray solid line). (d) Averaged ground penetrating radar (GPR)-derived soil water content (SWC) (colored dashed lines). (e) Soil water potential (SWP) at 140-cm depth (black dots). The vertical solid black line indicates sowing date, the vertical black dotted indicates flowering date, and vertical black dashed line indicates harvest date. The gray dashed frames indicate the GPR-derived SWC, which are shown in more detail in Figure 7.

where N is the number of GPR-derived SWCs, n_{SHP} is the number of optimized SHP, and SSR is the sum of squared residuals between measurements and model results. The AICc is used (instead of the AIC, Akaike, 1974) since the ratio between the number of GPR-derived SWCs and the number of optimized SHP (N/n_{SHP}) is smaller than 40 (Burnham & Anderson, 2004). The model with the lowest AICc values is deemed the best. Equation (10) demonstrates that the AICc's right-hand side penalizes the number of model parameters used. The AICc is advantageous over other statistical measures as it can be used even for a small number of observations N.

For estimating the resembled mean SWR functions of the 61 individual soil retention functions retrieved by the semi-3D sequential inversion, SWC/pressure head pairs of each individual of the 61 SWR functions were selected from full saturation to dryness (total of 1.000.000 data pairs) and used to fit a new set of SHP to those points (see Figure 5).

This procedure has been already applied by Montzka et al. (2017). As for the estimation of the hydraulic conductivity function, additional parameters such as K_s and λ are needed those have to be determined as well. As it is widely accepted that K_s and λ can be directly averaged, those parameters were averaged directly over the length of the rhizotubes.

3 | RESULTS AND DISCUSSION

3.1 | Field dataset for hydrological modeling

The precipitation data shown in Figure 3a indicated sporadic rain events, with fewer occurrences in October 2015 and mid-May 2016, and a higher number of rainfall events in late May and June. During this period, there were four events with rainfall over 10 mm per day within a 30-day span, and 8 days
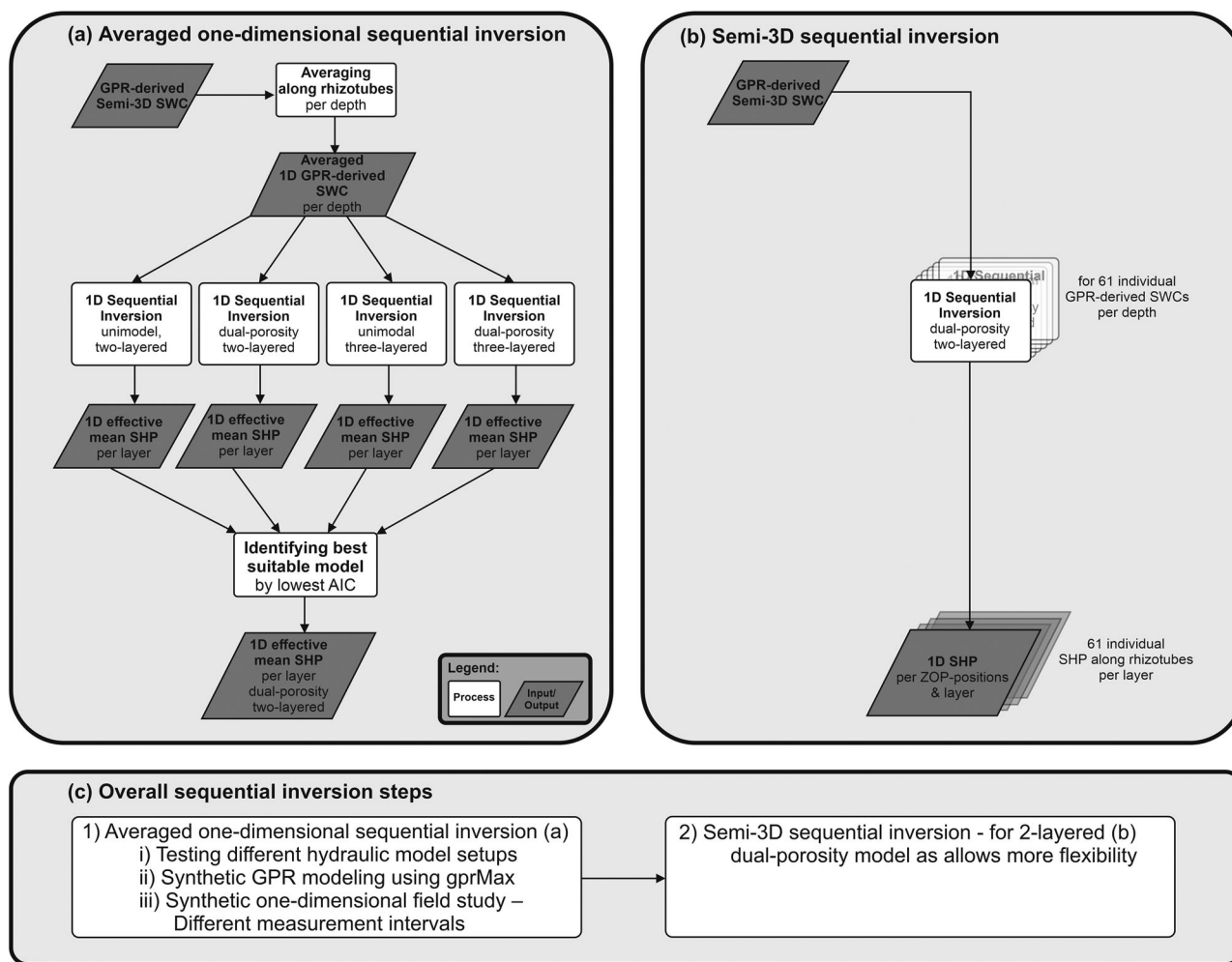
FIGURE 4 (a) Steps for the estimation of the averaged soil hydraulic parameters. (b) Steps for the estimation of the spatially distributed soil hydraulic parameters. (c) Overall sequential inversion steps. AIC, Akaike information criteria; GPR, ground penetrating radar; SHP, soil hydraulic parameters; SWC, soil water content; ZOP, zero-offset-profiling.

with over 10 mm of rainfall between October and mid-May. Potential evapotranspiration was at its lowest during winter, increasing in spring, and reaching its maximum during summer.

Based on the data from the root images, where we considered the maximum rooting depth as the depth where the first roots were detected in the root images at a given depth, root growth was determined and plotted in Figure 3b. Based on the root evolution, it became evident that the depth of root growth progressively increased until it reached a plateau during the flowering period. Since the rhizotubes were only installed until a depth of 1.2 m, root observation was feasible only up to 1.2 m. Given that wheat is a crop known for its deep-rooting nature (Thorup-Kristensen et al., 2009), we extrapolated the rooting depth to a depth of 1.4 m, whereby the slope of the growing curve over time was used for extrapolating. The LAI exhibited low values during the initial growing stages but showed a significant increase from mid-March to early May (refer Figure 3b). The LAI fluctuated around a

maximum between mid-May and early July, followed by a decrease toward the end of the growing season. Both the LAI and the rooting depth were considered to be zero after the harvest date, assuming no root activity after removal of the shoots. As described earlier, using Equations (4) and (5), we adjusted the crop transpiration using a crop coefficient. This crop coefficient was linearly interpolated, according to Figure 2. The respective dates for changing the crop coefficient were determined by the observed LAI pattern (see Figure 3c).

First, we explored the averaged GPR-derived SWC (arithmetic mean) values along the rhizotubes. This approach allowed us to analyze how SWC changes over time and at different depths (Figure 3d). Generally, lowest averaged SWCs were detected in the plow layer (0.2 m), with increasingly elevated SWCs in deeper zones of the soil profile. Moreover, the temporal variability decreased with increasing depth, as the dynamics stem primarily from the surface atmospheric conditions imposed, including evapotranspiration and precipitation.
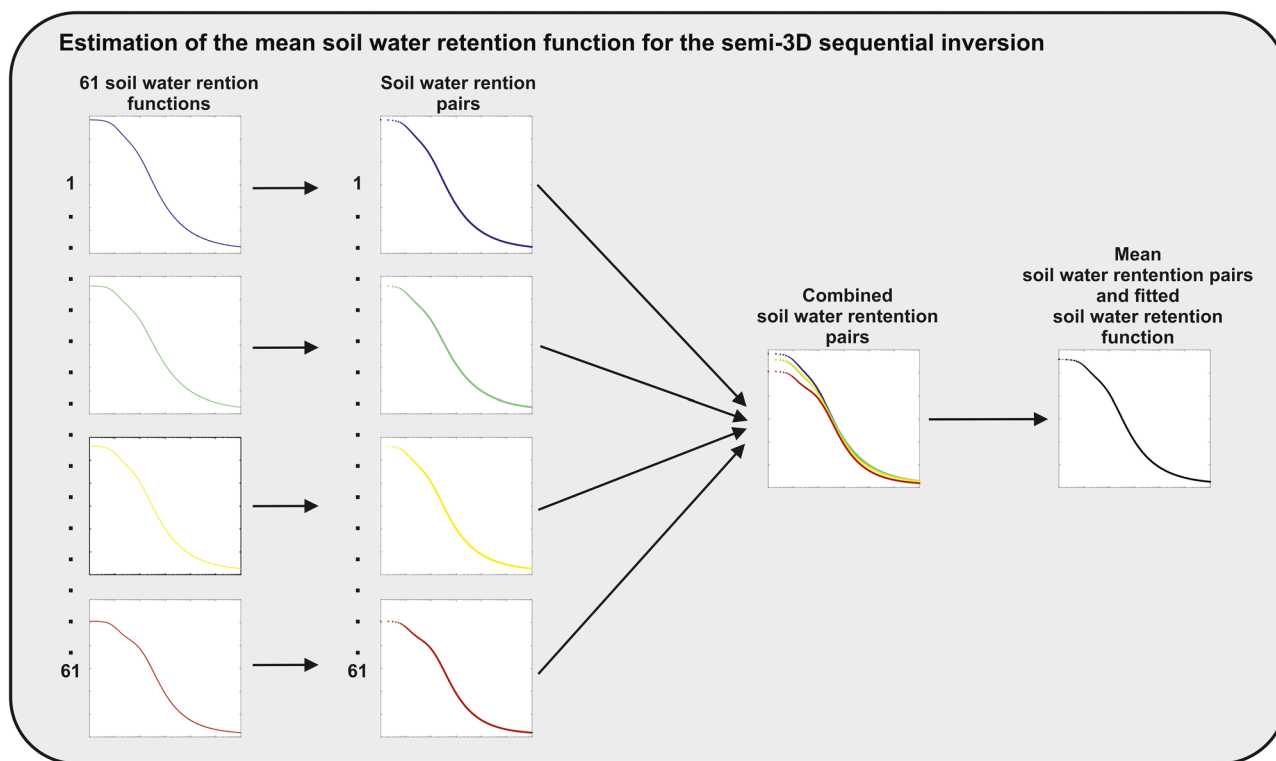
FIGURE 5 Estimation of soil water retention functions for the semi-3D (three-dimensional) sequential inversion.

Furthermore, heavy rainfall in June around flowering caused relatively high degree of saturation at 0.4-m depth. The averaged GPR-derived SWC (Figure 3d) showed a clear response to the precipitation and the evapotranspiration (Figure 3a). An increase in GPR-derived SWC was observed, such as the one on June 2 as a response to heavy rainfall. In contrast, a decrease in GPR-derived SWC was observed during drought events, such as on July 20. It is important to note that the differences in SWC between drier and wetter periods are not well expressed due to the fine-grained nature of the soil at the R_{LT} MR facility, exhibiting a large water retention even for extended dry periods during the summer month. Additionally, the GPR-derived SWC indicated near saturation at the depth of 1.2 m during the winter season, which are likely caused by stagnant water and not by high water tables as historical water table measurements in close vicinity of the facility indicated groundwater fluctuations between 3 and 5 m as mentioned by Jadoon et al. (2012).

The soil profile's lower boundary could be studied by analyzing soil matric potential values taken at a depth of 1.4 m near the MR facility (see Figure 3e). Generally, seasonal fluctuations occurred with noticeable soil matric potential increased during the winter months (October–February) and notably decreased toward the summer months (March–August), which reflected groundwater depletion and recharge throughout the year.

3.2 | Averaged one-dimensional sequential inversion

3.2.1 | Testing different hydrological model setups

As a first step, the averaged GPR-derived SWCs along the rhizotubes at each measurement depth were used in a sequential inversion, testing different model setups, namely, the unimodal 2-layered model, the unimodal 3-layered model, the dual-porosity 2-layered model, and the dual-porosity 3-layered model, respectively. The resulting SHP for the different model setups for the respective soil layers are given in Table 2. While visually comparing the modeled SWCs of the four optimized models (Figure 6), larger offsets during the spin-up period were noticed. Since the soil profile in the model needed to equilibrate to the atmospheric conditions, these larger offsets were expected but vanished until the date when first GPR measurements became available. Additionally, larger differences in modeled SWC between the individual models were found in the plow layer (between April 28 and May 28, and after harvest July 27) and the lowest depth of 1.2 m (more or less over the entire period after April 28). This showed different responses of the four models to the prescribed boundary conditions at the upper and lower boundary, respectively.

TABLE 2 Results for the 1D (one-dimensional) sequential inversion of the averaged ground penetrating radar (GPR)-derived soil water contents (SWCs), with boundaries set in the SCE-UA (Shuffled-Complex-Evolution algorithm) optimization and the optimized SHP(soil hydraulic parameters) values for the different models.

				SHP			
				Two-layered model		**Three-layered model**	
		Lower boundary	**Upper boundary**	**Unimodal**	**Dual-porosity**	**Unimodal**	**Dual-porosity**
Plow layer	θ_r (cm³ cm⁻³)	0	0.01	0.002	0.009	0.004	0.01
	θ_s (cm³ cm⁻³)	0.25	0.45	0.25	0.275	0.25	0.276
	α (cm⁻¹)	0.009	0.1	0.0795	0.0998	0.0546	0.099
	n (-)	1.1	3.0	1.118	2.789	1.129	1.998
	K_s (cm day⁻¹)	10	200	199.57	10.31	139.8	12.38
	λ (-)	−2	10	4.59	−1.28	6.39	−1.15
	ω_2 (-)	0.85	1	–	0.861	–	0.851
	α_2 (cm⁻¹)	0.001	0.01	–	0.0088	–	0.0091
	n_2 (-)	1.1	1.6	–	1.445	–	1.382
	RMSE (cm⁻³ cm⁻³)			0.034	0.0268	0.0345	0.0268
	AICc (-)			142	253	143	253
Subsoil layer1	θ_r (cm³ cm⁻³)	0	0.01	0.009	0.006	0.004	0.005
	θ_s (cm³ cm⁻³)	0.3	0.45	0.387	0.379	0.3927	0.366
	α (cm⁻¹)	0.008	0.1	0.0086	0.0299	0.013	0.0423
	n (-)	1.1	3.0	1.358	2.091	1.261	2.048
	K_s (cm day⁻¹)	0.8	200	159.52	192.51	107.88	133.04
	λ (-)	−2	10	−0.6	−0.06	0.1723	−1.88
	ω_2 (-)	0.85	1	–	1	–	0.957
	α_2 (cm⁻¹)	0.001	0.01	–	0.0061	–	0.0047
	n_2 (-)	1.1	1.6	–	1.501	–	1.495
	RMSE (cm⁻³ cm⁻³)			0.017	0.019	0.019	0.014
	AICc (-)			352	722	243	457
Subsoil layer2	θ_r (cm³ cm⁻³)	0	0.01	–	–	0.005	0.004
	θ_s (cm³ cm⁻³)	0.3	0.45	–	–	0.4	0.367
	α (cm⁻¹)	0.008	0.1	–	–	0.01	0.0552
	n (-)	1.1	3.0	–	–	1.166	1.964
	K_s (cm day⁻¹)	0.8	200	–	–	86.1778	156.67
	λ (-)	−2	10	–	–	1.74	0.61
	ω_2 (-)	0.85	1	–	–	–	0.999
	α_2 (cm⁻¹)	0.001	0.01	–	–	–	0.0015
	n_2 (-)	1.1	1.6	–	–	–	1.372
	RMSE (cm⁻³ cm⁻³)			–	–	0.023	0.017
	AICc (-)			–	–	127	236
Number of optimized parameters				12	18	18	27
Overall *RMSE* (cm⁻³ cm⁻³)				0.033	0.033	0.035	0.032
Overall *AICc* (-)				1918	3115	3129	4910

Note: For the selection of the best model, the RMSE and AICc were calculated for each soil layer individually and over all depths.

Abbreviations: AICc, corrected Akaike information criteria; RMSE; root mean square error; SHP, soil hydraulic parameters.

For the plow layer, we noticed that the two dual-porosity models showed minor differences between each other. On the other hand, the unimodal models indicated a different modeled SWCs, where the 2-layered model continuously showed larger SWCs than the 3-layered model, with an increase in the offset during the dry period in May with lower SWCs for the 3-layereds model. Interestingly, around the harvest date, we observed a noticeably higher SWC in the dual-porosity
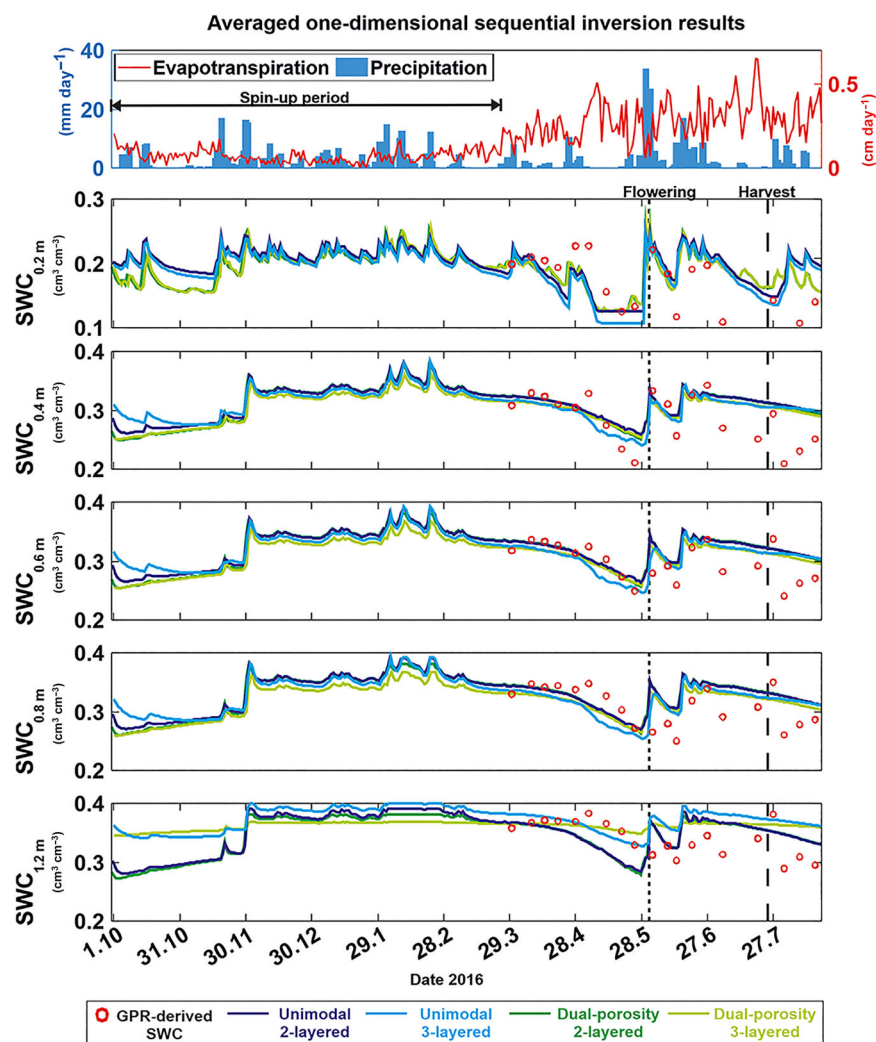
FIGURE 6 Results for the averaged one-dimensional (1D) sequential inversion. The uppermost plots show the atmospheric conditions (daily precipitation [blue bars], reference grass evapotranspiration [red line], and the black arrow indicates the spin-up period) followed by the different ground penetrating radar (GPR)-derived soil water content (SWC) measurement depths. The solid lines indicate the modeled SWC for the different model setups. The red circles indicate the averaged GPR-derived SWC. The vertical black dotted indicates flowering date and vertical black dashed line indicates harvest date.

models, and after the harvest, a significantly lower SWC compared to those predicted by the two unimodal models.

When looking at the subsoil depths, we noticed the differences between the individual models increased with increasing depth. The two dual-porosity models showed similar SWCs over the entire simulation period, whereas the unimodal 3-layered model showed the lowest SWCs during dry periods for all depth except at 1.2 m, where this model generally showed higher SWCs compared to the 2-layered cases. However, the lowest depth of 1.2 m showed a varying trend: the unimodal models and the dual-porosity 2-layered model predicted substantial differences in modeled SWC, whereas the dual-porosity 3-layered modeled SWCs did not change considerably throughout the modeling period.

When comparing the modeled and observed SWCs, it was difficult to distinguish which model best represented the observed SWCs over all depths as the modeled and observed SWC showed a wide range of offsets. Overall, Figure 6 showed that none of the utilized models perfectly represented the GPR-derived SWCs. A pattern of SWC underestimation during spring (March–April) and overestimation at later times

was also evident. Furthermore, all models exhibited less temporal SWC variability compared to the GPR-derived SWC, although they effectively captured the high rainfall events at all measurement depths.

Since these patterns and offsets made the visual comparison quite difficult, the AICc (Equation 10) and the root mean square error (RMSE) were calculated for the different models and soil layers individually and are listed in Table 2. As mentioned above, a low value in AICc indicated a good correlation between the modeled and observed SWC while penalizing a high number of optimized parameters. The unimodal 2-layered model had the lowest AICc value of 1918, considering the overall AICc for both layers (RMSE = 0.033 cm^{-3} cm^{-3}) (Table 2), indicating that this model was the best in terms of representing the measured SWCs and number fitted parameters. The second-best model was the dual-porosity 2-layered model, which had the same RMSE as the unimodal 2-layered model but slightly larger AICc (AICc = 3115) due to a larger number of fitted parameters. The unimodal 3-layered model closely followed with an AIC of 3129 and also slightly larger RMSE of 0.035 cm^{-3} cm^{-3}. Finally, the worst model was the

dual-porosity 3-layered model with an AICc of 4910 but with the lowest RMSE of 0.032, respectively. Here, it must be noted that the AICcs for the different models were relatively similar for the dual-porosity 2-layered and unimodal 3-layered case, whereby the RMSE differed with lower RMSE for the dual-porosity 2-layered case associated also with lower RMSE compared to the one for the dual-porosity 3-layered case. The ambiguous information content of the RMSE became clearer looking at the RMSE only to describe the goodness of fit to the data, when we looked at the dual-porosity 3-layered case, which showed the lowest RMSE of all cases but also the highest AICc due to large number of fitted parameters. Therefore, not accounting for the complexity of the model to describe the data (here the number of parameters fitted as done by the AICc) and to base the decision on lowest RMSE only will lead to a model selection, where the model complexity cannot be justified by the relatively small decrease in RMSE. To identify the most suitable model for further investigation (fitting the semi-3D SHP) of our soil system, we employed the following argumentation line: (1) the unimodal 3-layered model was not selected as it showed highest RMSE and second-worst AICc during the averaged 1D sequential inversion procedure and (2) the unimodal 2-layered model was not selected as per definition a dual-porosity model can also describe unimodal soil characteristics by setting the weighting factor $\omega 2$ to 1. This flexibility of the dual-porosity model could be already seen in the fitting results of the averaged 1D sequential inversion, where the dual-porosity model for the 2-layered model in the subsoil yielded an $\omega 2$ of 1, indicating unimodality. Finally, we rejected the 3-layered dual-porosity model, since the AICc for the averaged 1D sequential inversion was considerably larger than those of the other cases. Therefore, we selected the 2-layered dual-porosity model as most suitable for fitting the distributed semi-3D SHPs.

3.2.2 | Synthetic GPR modeling using gprMax

During heavy rainfall events or irrigation, sharp gradients in the SWC profile can occur, leading to incorrect estimations of GPR-derived SWC when the first arrival time (first break) analysis is used (Yu et al., 2021). To assess if this occurred for the natural field climatic conditions of our study, a synthetic modeling study was carried out utilizing the three-dimensional finite difference time domain software gprMax (Warren et al., 2016). For the simulation, we used the modeled SWC profiles acquired for the averaged one-dimensional sequential inversion using the dual-porosity 2-layered model (refer to Table 2 and Figure 6). From these modeled SWC profiles, we computed the distribution of relative dielectric permittivity throughout the entire depth of the soil profile in 0.02 m increments for the 20 days in which GPR data were collected in the field. A replica of the MR facility was set

up using gprMax, where for each of the five measurement depths, a pair of rhizotubes with a spacing of 0.75 m between the receiver and transmitter antennae was incorporated into the model and used to compute the EM field components at the antennae locations. The soil's electrical conductivity σ remained constant at 10 mS m^{-1}, while the source pulse was set to a Ricker wavelet centered at 200 MHz. The EM waves generated from the calculations were processed similar to the one used for field measurements. The first break was determined (see Figure 7a), and from this, the EM travel time, EM wave velocity, relative dielectric permittivity, and finally the SWC were calculated. This entire process was repeated for each depth at each timestep. The SWC profiles resulting from this processing were finally compared to both the GPR-derived SWC measurements and the modeled SWC profiles employing HYDRUS-1D (see Figure 7b). Comparing the SWC for the four selected dates, one could see that the SWC simulated by the use of gprMax correlated with the modeled SWC profile especially at greater depth between 0.6 and 1.2 m, indicating the suitability of the first arrival time approach for estimating GPR-derived SWC. At depths of 0.2 and 0.4 m, there is an observable offset between the modeled SWC profile and SWC simulated in gprMax. This may be attributed to the difference in SWC between the plow and subsoil layer, resulting in notable differences in SWC values over short distances, whereby the differences were still quite small. Furthermore, those differences might be also caused by the fact that the measurements were acquired near the interface between the air and soil and might therefore be affected by the critically refracted air and direct waves, as mentioned earlier. Looking at all measurement dates (not all data shown here), the infiltration water after rainfall events did not create considerably sharp gradients in SWC that could impact SWC estimation from picking the first arrival. This exercise therefore demonstrates that the first arrival time analysis was suitable to estimate the modeled SWC and that a full waveform coupled inversion as done by Yu et al. (2021).

3.2.3 | Synthetic one-dimensional field study—Different measurement intervals

The second potential drawback to be discussed was the adequacy of the number of GPR-derived SWC measurements necessary to accurately estimate the SHP. As indicated earlier, our field experiments contained 20 measurements over a period of 6 months. As such, it is uncertain whether this data density was enough to constrain the sequential inversion. Therefore, two sets of synthetic GPR-derived SWC measurements were created. The first one, where the 20 available field experiment measurement days were selected and a second one, where daily measurements over a period of 6 months (323 days) were selected from the HYDRUS-1D time series,
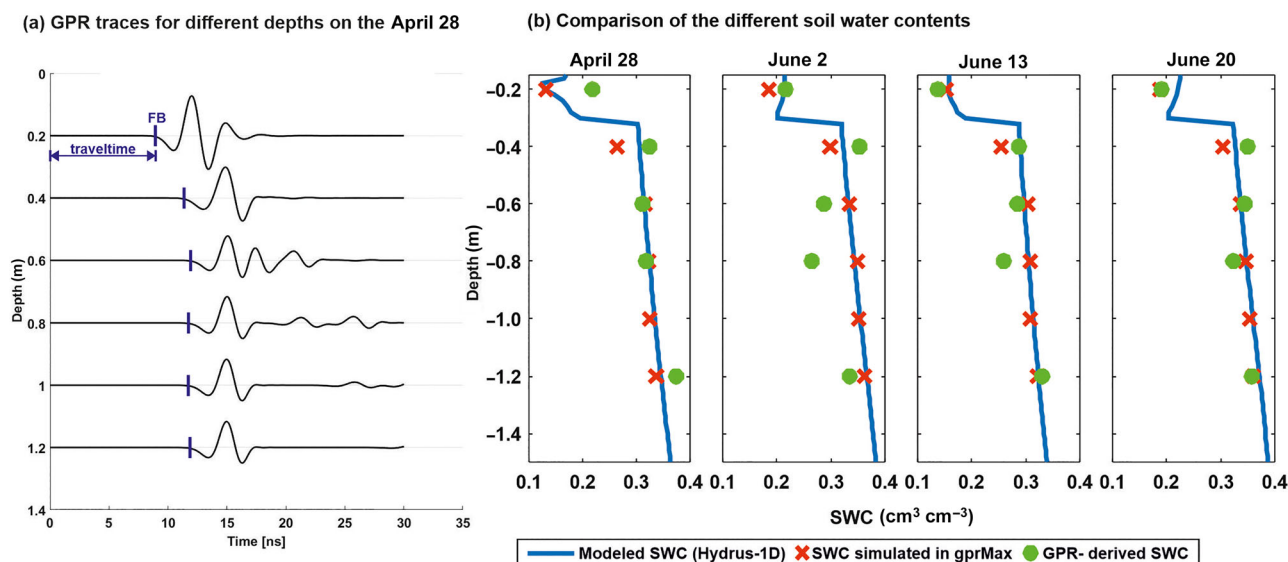
FIGURE 7 (a) Synthetic ground penetrating radar (GPR) traces modeled using gprMax (Warren et al., 2016) for the different depths for the April 28, 2016, where the black lines indicate the simulated electromagnetic (EM) waves per depths and the blue marks represent the first break (FB) of the simulated EM waves. (b) SWC (soil water content) profile comparison for four exemplary GPR days (April 28, June 2, June 13, and June 20 in 2016). The blues line presents the modeled SWC profile resulting from the averaged one-dimensional (1D) sequential inversion, the red crosses indicated the gprMax-derived SWC, and the green circles represent the measured GPR-derived SWC.

using the SHP in Table 2 for the unimodal 2-layered model, as "original" input SHP. In this study, we used the simplest model (unimodal 2-layered), which contained lowest number of parameters and also adjusted the search range (feasible parameter space) for the optimization, to keep computation time low. For each of the two scenarios (20 measurement days or daily measurements), a sequential inversion was performed and the resulting SHP and the respective coefficient of determination R^2 are shown in Table A1. For both scenarios, the sequential inversion returned the "original" input SHP used in the forward model. Hereby, the model fed with the 20 GPR measurements days taken from the field experiment resulted in R^2 of 1, while the model based on daily SWC inputs resulted in R^2 of 1 also. Therefore, it can be concluded that the 20 available measurement days provide adequate information to constrain the sequential inversion. For more details, about the results of this synthetic study, we refer to Figure A1 and Table A1.

3.3 | Semi-3D sequential inversion

To investigate the horizontal spatial variability of the SHP along the rhizotubes, the GPR-derived SWCs for each measurement day could be visualized and examined over time for all 61 measurement positions. Figure 8 displays the horizontal depth planes of three selected different measurement dates (April 28, June 20, and August 1). Typically, the lowest SWCs were detected in the plow layer (0.2 m), while the deeper soil profile showed systematically higher values. Temporal vari-

ability decreased with increasing depth due to atmospheric conditions at the surface. Patches of GPR-derived SWC variability demonstrated that SWCs are heterogeneous, leading to the hypothesis that the underlying soil characteristics are spatially variable (Figure 8). To explore the spatial variability of the SHP, 61 individual sequential inversions were performed along the length of the rhizotubes for each depth. Based on the previous sequential inversion, using the averaged GPR-derived SWC, the 2-layered setup, consisting of a plow (topsoil) and a subsoil layer, and a dual-porosity model was used. Since bimodality may exist within the soil hydraulic characteristics, excluding dual porosity a priori during inversion was not advised. Additionally, the dual-porosity function allowed for flexibility in yielding unimodal characteristic if the weighting factor $\omega2$ is close to or equals 1 (refer to Equation 10). After inverting the SHPs to all GPR-derived SWCs for all individual positions within the rhizotubes located in the plow and subsoil layers, the SWR and hydraulic conductivity curves were plotted in Figure 9. As depicted in the figure, we observed a noticeable dual-porosity pattern in the wet range for the plow layer (Figure 9a,c), while the soil characteristics for the subsoil layer displayed a more unimodal pattern (Figure 9b,d). The dual-porosity nature of the plow layer and the unimodal nature of the subsoil layer were also observed in the 1D inversion.

To explore the dual-porosity nature of both soil layers in more detail, a histogram of the weighting factor $\omega2$ was plotted in Figure 10. For the plow layer, there was almost no spread in the weighting factor $\omega2$, with 59 of the models having an $\omega2$ between 0.85 and 0.86, and only two between 0.86
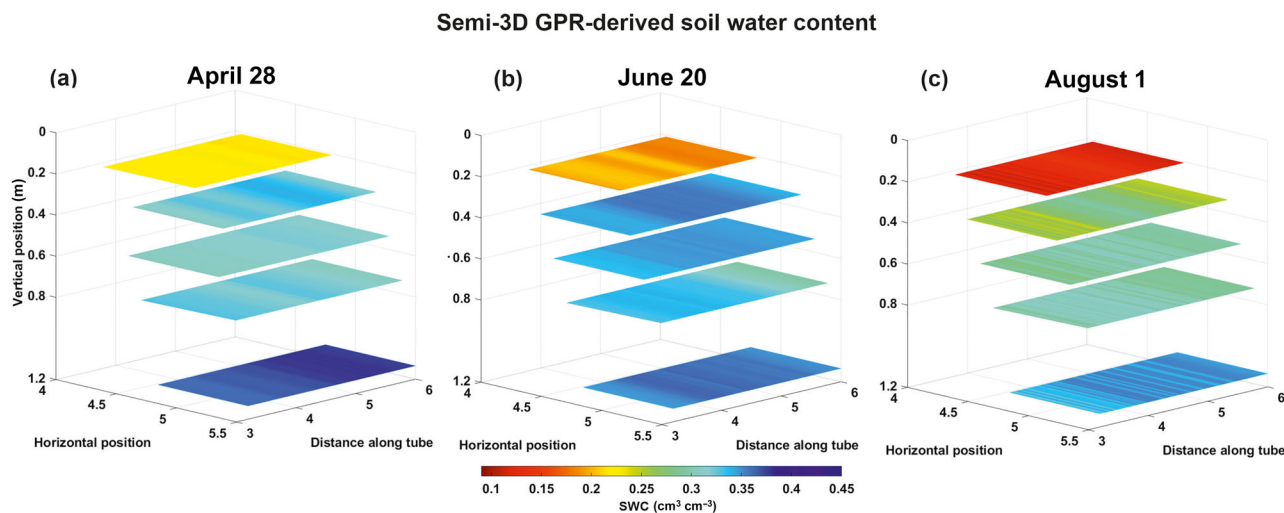
Semi-3D GPR-derived soil water content

FIGURE 8 Ground penetrating radar (GPR)-derived soil water content (SWC) along the rhizotubes for three selected dates during the crop growing season: (a) April 28, (b) June 20, and (c) August 1 in 2016.

and 0.87. Hence, the plow layer showed a bimodality of at least 15%. In contrast, for the subsoil layer, $\omega 2$ was much more variable, ranging from 0.88 to 1, and was highly skewed toward 1, indicating low bimodality to near unimodality. The estimated SHP for the 61 positions along the rhizotubes are shown in Figure 11, where the subfigure include not only the estimated parameter for each individual GPR measurement positions but also the averaged SHP calculated from the individually optimized parameters along the rhizotubes (here denoted as mean semi-3D results, see Figure 11), as well as the results of the sequential inversion based on the averaged GPR-derived SWCs along the rhizotubes (here denoted as averaged 1D results).

For the plow layer, there was a deterministic trend present for the soil matrix parameters α_2 and n_2 but also a trend in θ_s (see Figure 11a). For θ_s, lower values were detectable in the first 3.4 m, peaking after between 3.4 and 3.8 m and leveled out at levels of the average θ_s until 5.2 m. Beyond that, the θ_s again increased. For α_2, the values were generally below the inversion results based on the averaged GPR-derived SWC between 3 and ~4.0 m. In contrast, between ~4 and 6 m, the values were above this averaged GPR-derived SWC. This trend was reversed for n_2, suggesting a negative correlation between matrix α and n as already found by Zhang et al. (2022) for laboratory derived data. A similar trend could be seen for the subsoil layer in Figure 11b.

To investigate this further, Figure 12 shows the negative correlation between α_2 and n_2 for both soil layers. The R^2 gave values of 0.4 and 0.53 for the plow and subsoil layer, respectively. When analyzing K_s and λ within the plow layer, we could notice similar patterns along the locations of the rhizotubes, where high values for both parameters above the mean of the semi-3D results, between 3.0 and 3.7 m, were present, which then decreased below the mean toward 5.1 m. Between

5.1 and 6.0 m, a slight increase was present toward values around the mean. This similar trend of K_s and λ suggested a correlation between those parameters (see Figure B1). Generally spoken, increasing K_s while decreasing λ will lead to more or less the same conductivity function as decreasing K_s while increasing λ, and therefore, a correlation can be assumed. For all other parameters estimated in for the plow layer (θ_r, α_1, and n_1), no clear trend was visible.

In contrast to the plow layer, a clear trend along the rhizotube measurement positions for the estimated θ_s could be found in the subsoil layer (Figure 11b), where the values between 3 and 4.4 m (roughly at the center of the rhizotube) were higher than 0.37 cm^3 cm^{-3} and decreased steadily toward the end of the rhizotube. The remaining parameters (θ_r, K_s, λ, α_1, and n_1) did not follow a clear trend, and only for ω_2, α_2, and n_2, high variability in the first half of the rhizotube was noticeable, which was smaller for the second half along the tube. Finally, there was no correlation between K_s and λ compared what was present in the plow layer.

In a final step, we compared the effective (mean) SHPs for the MR facility. On the one hand, a set of SHPs was estimated based on the averaged one-dimensional GPR-derived SWCs (averaged 1D) and on the other hand, the SHPs were estimated from ensembled mean SWR pairs (mean semi 3D) of the individual functions, as mentioned above and described in Figure 5. The offset and the direction of the offset between the different values (averaged 1D and mean semi-1D) was quite variable. In some cases, the values were very similar, for example, θ_s and n_2 within the plow layer (see Figure 11), whereas within the subsoil layer, the values between the different averaged SHP were quite large, for n_1 and n_2 but also for $\omega 2$. Looking at all averaged 1D and mean semi-3D SHP, no clear trend could be detected.

Soil water retention and absolute hydraulic conductivity function for the semi-3D sequential inversion
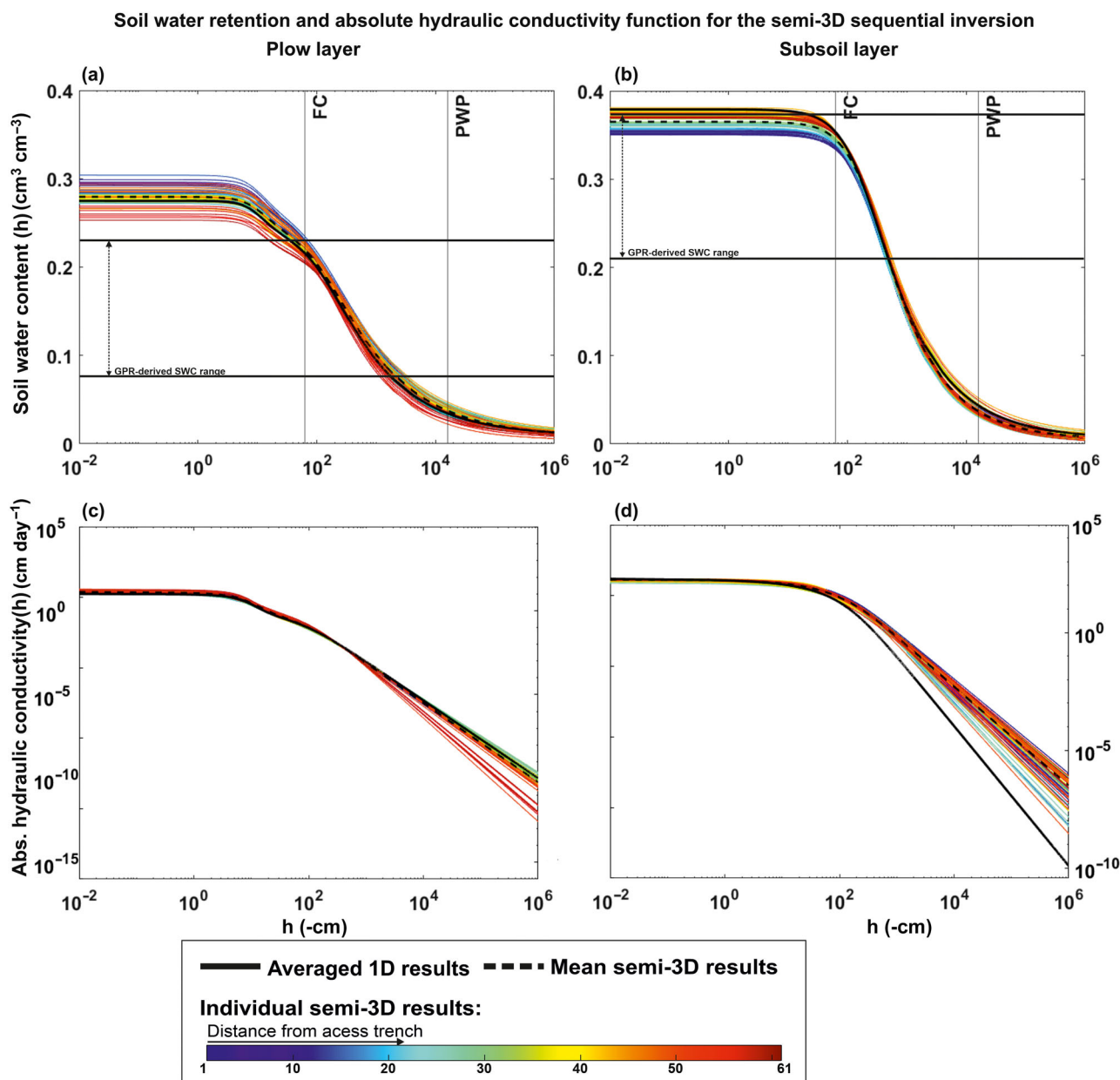

FIGURE 9 Soil water retention (a and b) and relative hydraulic conductivity function (c and d) for the plow and subsoil layer, respectively. The different colors represent the individual results along the rhizotubes, where the blue colors are the results closest to the access trench. The black dashed line and the black solid line indicate the results of the averaged one-dimensional (1D) sequential inversion results and the mean of semi-3D (three-dimensional) sequential inversion results, respectively. The vertical lines in the soil water retention functions (a and b) represent the pressure head and the corresponding soil water content values at field capacity (FC) and permanent wilting point (PWP). The horizontal lines in the soil water retention functions (a and b) represent the GPR-SWC (ground penetrating radar-soil water content) range for the measurements.

Information on the soil characteristics FC, PWP, and PAW is often required in crop growth studies (Kersebaum et al., 2015). The variability of these parameters can significantly affect plant performance under conditions such as water stress or nutrient deficiency and, consequently, crop productivity including yield (Aggarwal, 1995; Van Keulen et al., 1987). The SWC at FC, PWP, and PAW was individually calculated for each GPR-derived SWC measurement position along the rhizotubes, as shown in Figure 13. Furthermore, we incorpo-

rated the SWC at FC, PWP, and PAW obtained through the inversion of the averaged 1D GPR-derived SWC and the mean semi-3D inversion results. The SWC at PWP (Figure 13b) and PAW (Figure 13c) indicated a more or less symmetrical distribution in the plow layer, while for the FC (Figure 13a) also, a symmetrical distribution in the subsoil layer was visible. However, the remaining parameters were skewed toward the lower SWC range. Furthermore, the soil characteristics of individual layers could be compared. The SWC at FC is

FIGURE 10 Histogram of the weighting factor ω_2 for (a) the plow layer and (b) the subsoil layer for all 61 ground penetrating radar (GPR) locations.
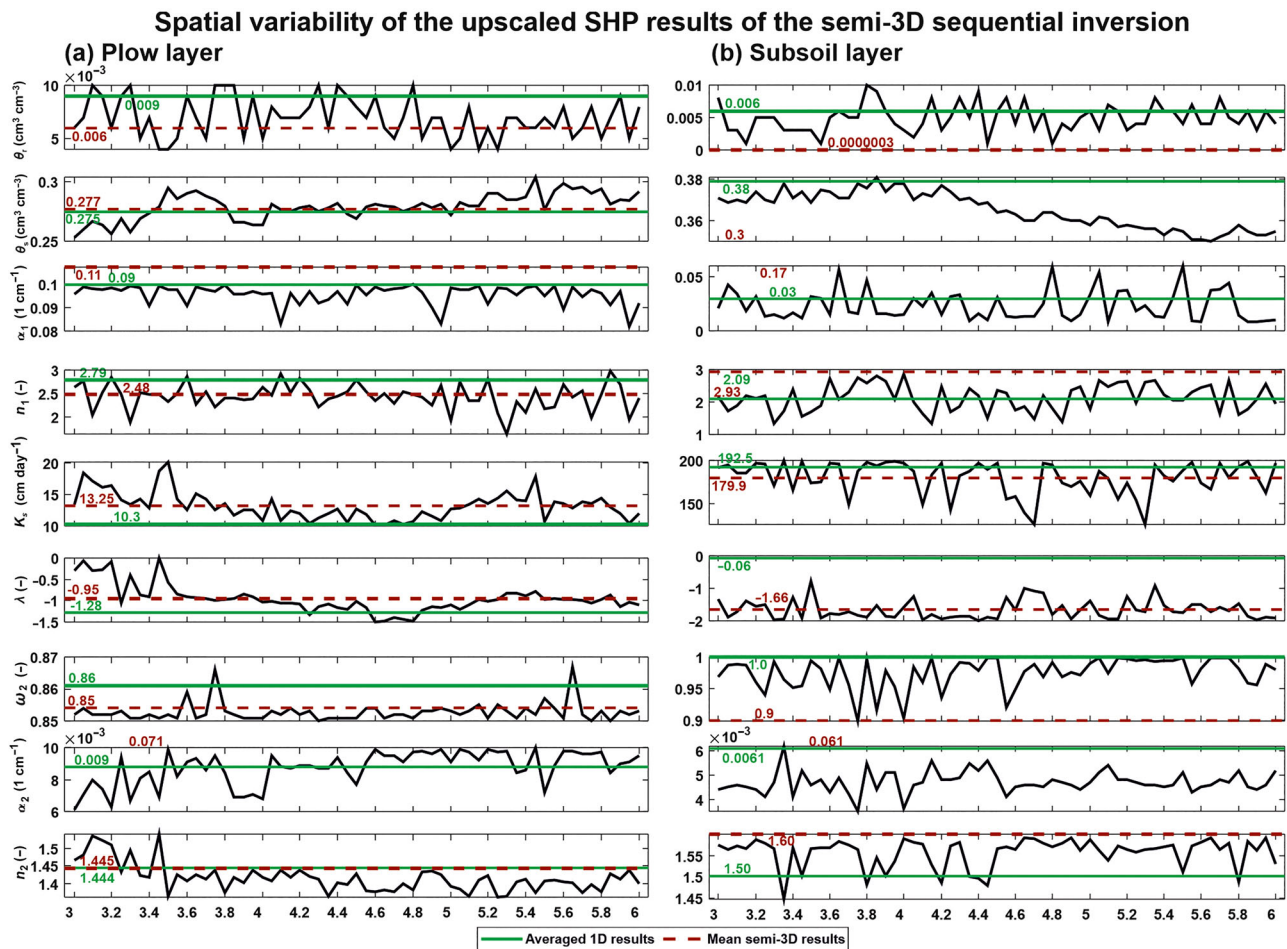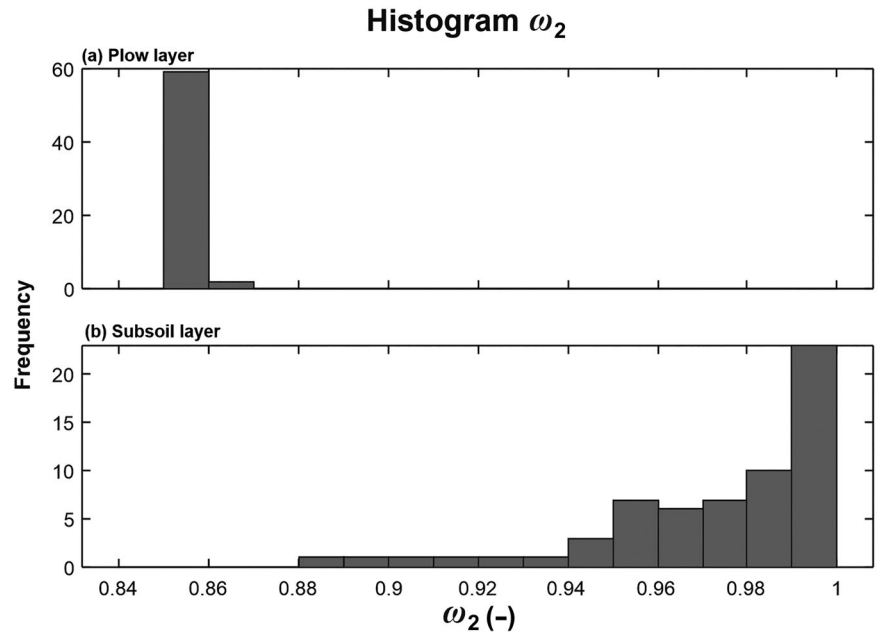

FIGURE 11 (a and b) The semi-3D (three-dimensional) sequential inversion results for the plow layer and the subsoil layer, respectively. The individual subplots indicate the results along the rhizotube for the soil hydraulic parameters. The black solid lines show the individual results along the rhizotubes, the red dashed line indicates the mean of the semi-3D results, and the green solid line indicates the averaged one-dimensional (1D) inversion results. Note, for some SHP, the mean values were out of range to show values along the rhizotubes; hence, only the corresponding values are indicated.
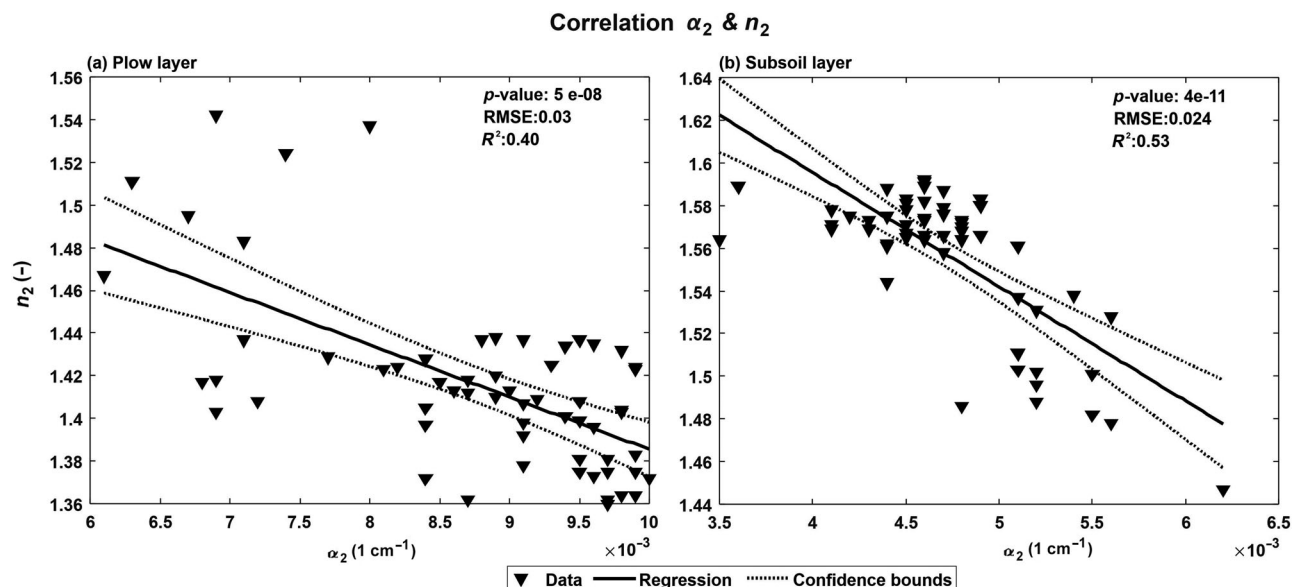
Correlation α_2 & n_2

FIGURE 12 Correlation between α_2 and n_2 for (a) plow layer and (b) the subsoil layer based on the inversion along the 61 locations within each rhizotube. RMSE; root mean square error.
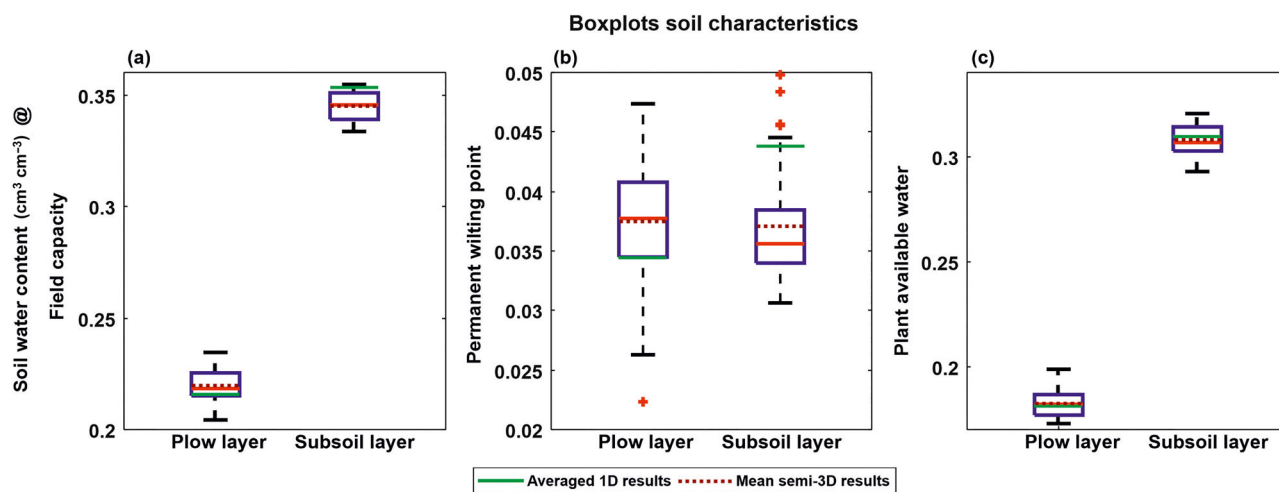

FIGURE 13 Boxplot for the semi-3D (three-dimensional) sequential inversion results for the soil water content at field capacity (a), permanent wilting point (b), and plant available water (c). The green solid line indicates the values based on averaged one-dimensional (1D) sequential inversion results and the dark red dashed line indicates the mean semi-3D inversion result. The red solid line shows the median from the semi-3D inversion results, the blue box the 25th and 75th percentile, the black whiskers the most extreme data points not considered as outliers, and stars the outliers.

lower for the plow layer and exhibited slightly more variability in the subsoil layer. The lower FC for the plow layer was consistent with lower saturated water content θ_s (porosity) of this layer, likely caused by repeated tillage and destruction of soil structure. Conversely, the SWC at PWP was slightly higher and more variable for the plow layer. Three outliers were observed for the subsoil layer, which were very different from the other values, while there was only one outlier at the lower end of the range for the plow layer. The SWC at PAW in the plow layer was lower compared to that of the subsoil layer. Furthermore, there was a higher variabil-

ity in the subsoil layer, as indicated by a wider range between the 25th and 75th percentiles. When comparing the boxplot median to the results from the averaged 1D GPR-derived for the PAW, it was evident that the inversion of the averaged one-dimensional GPR-derived SWC yielded a PAW value outside the quartiles for the subsoil layer. The same also held for the FC, indicating that even small differences in the SHP as shown in Figure 11 might lead to some substantial difference in the derived secondary soil properties PWP and FC. Additionally, for the averaged one-dimensional GPR-derived PAW, the value was near the upper whisker, indicating considerable

variability beyond the upper quartile. Meanwhile, for SWC at FC and PWP in the plow layer, the results of the mean semi-3D were located close to the lower quartile, indicating that the secondary soil properties might vary substantially between the two different averaging procedures. As the PAW obtained from mean semi-3D (of the ensembles curves, as shown in Figure 5) for the top and subsoil layer but also the FC for the subsoil layer were closer to the median of the boxplots, compared to averaged 1D GPR results, one can conclude that averaging the individual soil hydraulic characteristics and fitting an ensembled new curve to those data yielded better results as averaging the SWCs beforehand and inverting on those. Finally, the results revealed that variability in the SHPs was partly substantial at the different layers and that neglecting this variability might lead to SHPs, which might not be appropriate to be used in modeling the soil–plant interactions at different scales, especially at a fine scale.

4 | SUMMARY AND CONCLUSION

In this study, the SHP were estimated using the unimodal and dual-porosity MvG model. The method relied on time-lapse 200-MHz horizontal ZOP crosshole GPR-derived data, which were used to determine the SWC over the course of a winter wheat cropping season.

The results showed that the hydrogeophysical sequential inversion approach can be used to estimate the SHP reliably for effective SHP based on averaging the SWCs along the rhizotubes prior inversion. The results also indicate that the GPR measurements provide sufficient information details to estimate the SHP for the plow (topsoil) and subsoil layer, with the added capability of also estimating the parameters of dual-porosity soil hydraulic characteristics. Regardless of the good fit of the modeled SWCs, some discrepancies were still detectable, where the modeled SWCs showed in general less variability than the GPR measured ones. To ensure that this discrepancy was not caused by the method how SWCs were derived from GPR data (i.e., first arrival time), a synthetic modeling study was performed, whereby the calibrated model was utilized in conjunction with gprMax, a three-dimensional finite difference time domain software (Warren et al., 2016) to simulate EM of the system. Those EM waves were then analyzed in the same manner as those measured in the field and the results indicated that the gathered field GPR data can be analyzed using standard picking of the first arrival times and that the absence of sharp gradients in SWC will allow this simple data analysis as suggested earlier by Yu et al. (2021).

In the next step, a semi-3D sequential inversion of the SHP was performed, using the individual GPR-derived SWCs from the different locations along the rhizotubes ($N = 61$ per rhizotube). The results showed that the calculated SHP vary across the locations of the rhizotubes. Additionally, the

obtained semi-3D SHP differ from the SHPs estimated using the mean GPR-derived SWC along the rhizotubes, as well as from the calculated mean of the upscaled SHPs. The latter was obtained by fitting the soil hydraulic properties to the average SWR function. From the SWR functions for the different methods used to estimate the SHP (inversion of the averaged GPR-derived SWCs and inversion of SWC along individual locations along the rhizotubes or averaging of the latter), further soil water characteristics were estimated, including FC, PWP, and the PAW. The results showed that the different techniques for calculating the SHPs also yield different SWCs at FC, PWP, and PAW and that averaging SWC prior inversion will lead to larger differences compared to estimating a mean set of SHPs based on the ensemble of individually estimated soil hydraulic characteristics. For future research, we would recommend analyzing the effect of the different SHP estimated on dynamic root-soil or crop growth models. Another consideration would be how these small-scale heterogeneities would impact biogeochemical processes like GHG production and emissions using an appropriate biogeochemical model.

AUTHOR CONTRIBUTIONS

Lena Lärm: Conceptualization; data curation; formal analysis; methodology; validation; visualization; writing—original draft. **Lutz Weihermüller**: Conceptualization; formal analysis; methodology; supervision; validation; visualization; writing—original draft; writing—review and editing. **Jan Rödder**: Formal analysis. **Jan van der Kruk**: Supervision; writing—original draft. **Harry Vereecken**: Supervision; writing—original draft. **Anja Klotzsche**: Conceptualization; funding acquisition; methodology; project administration; resources; supervision; writing—original draft.

CONFLICT OF INTEREST STATEMENT

The authors declare no conflicts of interest.

ORCID
Lena Lärm https://orcid.org/0000-0002-0633-4293
Lutz Weihermüller https://orcid.org/0000-0003-1991-7735
Jan van der Kruk https://orcid.org/0000-0003-2348-1436
Harry Vereecken https://orcid.org/0000-0002-8051-8517
Anja Klotzsche https://orcid.org/0000-0002-7021-5045

REFERENCES

Aggarwal, P. K. (1995). Uncertainties in crop, soil and weather inputs used in growth models: Implications for simulated outputs and their applications. *Agricultural Systems*, *48*, 361–384. https://doi.org/10.1016/0308-521x(94)00018-m

Akaike, H. (1974). A new look at the statistical model identification. *IEEE Transactions on Automatic Control*, *19*, 716–723. https://doi.org/10.1109/tac.1974.1100705

Allen, R. G., Pereira, L. S., Raes, D., & Smith, M. (1998). *Crop evapotranspiration* (FAO irrigation and drainage paper No. 56). Food and Agriculture Organization of the United Nations.

Altdorff, D., von Hebel, C., Borchard, N., van der Kruk, J., Bogena, H. R., Vereecken, H., & Huisman, J. A. (2017). Potential of catchment-wide soil water content prediction using electromagnetic induction in a forest ecosystem. *Environmental Earth Sciences*, *76*, Article 111. https://doi.org/10.1007/s12665-016-6361-3

Amsili, J. P., van Es, H. M., & Schindelbeck, R. R. (2024). Pedotransfer functions for field capacity, permanent wilting point, and available water capacity based on random forest models for routine soil health analysis. *Communications in Soil Science and Plant Analysis*, *55*, 1967–1984. https://doi.org/10.1080/00103624.2024.2336573

Archie, G. E. (1942). The electrical resistivity log as an aid in determining some reservoir characteristics. *Transactions of the AIME*, *146*, 54–62. https://doi.org/10.2118/942054-g

Bauer, F. M., Lärm, L., Morandage, S., Lobet, G., Vanderborght, J., Vereecken, H., & Schnepf, A. (2022). Development and validation of a deep learning based automated minirhizotron image analysis pipeline. *Plant Phenomics*, *2022*, Article 9758532. https://doi.org/10.34133/2022/9758532

Bauer, J., Weihermüller, L., Huisman, J. A., Herbst, M., Graf, A., Séquaris, J. M., & Vereecken, H. (2011). Inverse determination of heterotrophic soil respiration response to temperature and water content under field conditions. *Biogeochemistry*, *108*(1–3), 119–134. https://doi.org/10.1007/s10533-011-9583-1

Bauke, S. L., Amelung, W., Bol, R., Brandt, L., Brüggemann, N., Kandeler, E., & Vereecken, H. (2022). Soil water status shapes nutrient cycling in agroecosystems from micrometer to landscape scales. *Journal of Plant Nutrition and Soil Science*, *185*, 773–792. https://doi.org/10.1002/jpln.202200357

Beaujean, J., Nguyen, F., Kemna, A., Antonsson, A., & Engesgaard, P. (2014). Calibration of seawater intrusion models: Inverse parameter estimation using surface electrical resistivity tomography and borehole data. *Water Resources Research*, *50*, 6828–6849. https://doi.org/10.1002/2013wr014020

Beff, L., Günther, T., Vandoorne, B., Couvreur, V., & Javaux, M. (2012). Three-dimensional monitoring of soil water content in a maize field using electrical resistivity tomography. *Hydrology and Earth System Sciences Discussions*, *9*, 8535–8578. https://doi.org/10.5194/hessd-9-8535-2012

Bogena, H. R., Huisman, J. A., Oberdörster, C., & Vereecken, H. (2007). Evaluation of a low-cost soil water content sensor for wireless network applications. *Journal of Hydrology*, *344*, 32–42. https://doi.org/10.1016/j.jhydrol.2007.06.032

Bogena, H. R., Montzka, C., Huisman, J. A., Graf, A., Schmidt, M., Stockinger, M., & Vereecken, H. (2018). The TERENO-Rur hydrological observatory: A multiscale multi-compartment research platform for the advancement of hydrological science. *Vadose Zone Journal*, *17*, 180055. https://doi.org/10.2136/vzj2018.03.0055

Brogi, C., Huisman, J. A., Pätzold, S., von Hebel, C., Weihermüller, L., Kaufmann, M. S., van der Kruk, J., & Vereecken, H. (2019). Large-scale soil mapping using multi-configuration EMI and supervised image classification. *Geoderma*, *335*, 133–148. https://doi.org/10.1016/j.geoderma.2018.08.001

Brosten, T. R., Day-Lewis, F. D., Schultz, G. M., Curtis, G. P., & Lane, J. W. (2011). Inversion of multi-frequency electromagnetic induction data for 3D characterization of hydraulic conductivity. *Journal of Applied Geophysics*, *73*, 323–335. https://doi.org/10.1016/j.jappgeo.2011.02.004

Brunet, P., Clément, R., & Bouvier, C. (2010). Monitoring soil water content and deficit using electrical resistivity tomography (ERT)—A case study in the Cevennes area, France. *Journal of Hydrology*, *380*, 146–153. https://doi.org/10.1016/j.jhydrol.2009.10.032

Burnham, K. P., & Anderson, D. R. (2004). Multimodel inference: Understanding AIC and BIC in model selection. *Sociological Methods & Research*, *33*, 261–304. https://doi.org/10.1177/0049124104268644</./bib>

Busch, S., Weihermüller, L., Huisman, J. A., Steelman, C. M., Endres, A. L., Vereecken, H., & van der Kruk, J. (2013). Coupled hydrogeophysical inversion of time-lapse surface GPR data to estimate hydraulic properties of a layered subsurface. *Water Resources Research*, *49*, 8480–8494. https://doi.org/10.1002/2013wr013992

Cai, G., Vanderborght, J., Klotzsche, A., van der Kruk, J., Neumann, J., Hermes, N., & Vereecken, H. (2016). Construction of minirhizotron facilities for investigating root zone processes. *Vadose Zone Journal*, *15*, 1–13. https://doi.org/10.2136/vzj2016.05.0043

Camporese, M., Cassiani, G., Deiana, R., Salandin, P., & Binley, A. (2015). Coupled and uncoupled hydrogeophysical inversions using ensemble Kalman filter assimilation of ERT-monitored tracer test data. *Water Resources Research*, *51*, 3277–3291. https://doi.org/10.1002/2014wr016017

Cassiani, G., Ursino, N., Deiana, R., Vignoli, G., Boaga, J., Rossi, M., & Werban, U. (2012). Noninvasive monitoring of soil static characteristics and dynamic states: A case study highlighting vegetation effects on agricultural land. *Vadose Zone Journal*, *11*, vzj2011.0195. https://doi.org/10.2136/vzj2011.0195

Claes, N., Paige, G. B., Grana, D., & Parsekian, A. D. (2020). Parameterization of a hydrologic model with geophysical data to simulate observed subsurface return flow paths. *Vadose Zone Journal*, *19*, e20024. https://doi.org/10.1002/vzj2.20024

Corwin, D. L., & Lesch, S. M. (2005). Apparent soil electrical conductivity measurements in agriculture. *Computers and Electronics in Agriculture*, *46*, 11–43. https://doi.org/10.1016/j.compag.2004.10.005

Doetsch, J., Linde, N., Vogt, T., Binley, A., & Green, A. G. (2012). Imaging and quantifying salt-tracer transport in a riparian groundwater system by means of 3D ERT monitoring. *GEOPHYSICS*, *77*(5), B207–B218. https://doi.org/10.1190/geo2012-0046.1

Doolittle, J. A., & Brevik, E. C. (2014). The use of electromagnetic induction techniques in soils studies. *Geoderma*, *223–225*, 33–45. https://doi.org/10.1016/j.geoderma.2014.01.027

Duan, Q., Sorooshian, S., & Gupta, V. K. (1994). Optimal use of the SCE-UA global optimization method for calibrating watershed models. *Journal of Hydrology*, *158*, 265–284. https://doi.org/10.1016/0022-1694(94)90057-4

Duan, Q. Y., Gupta, V. K., & Sorooshian, S. (1993). Shuffled complex evolution approach for effective and efficient global minimization. *Journal of Optimization Theory and Applications*, *76*, 501–521. https://doi.org/10.1007/bf00939380

Durner, W. (1994). Hydraulic conductivity estimation for soils with heterogeneous pore structure. *Water Resources Research*, *30*, 211–223. https://doi.org/10.1029/93wr02676

Durner, W., & Lipsius, K. (2005). *Determining soil hydraulic properties*. John Wiley & Sons, Ltd. https://doi.org/10.1002/0470848944.hsa077b

Farmani, M. B., Kitterød, N., & Keers, H. (2008). Inverse modeling of unsaturated flow parameters using dynamic geological structure conditioned by GPR tomography. *Water Resources Research*, *44*(8). https://doi.org/10.1029/2007wr006251

Feddes, R. A., Bresler, E., & Neuman, S. P. (1974). Field test of a modified numerical model for water uptake by root systems. *Water Resources Research*, *10*, 1199–1206. https://doi.org/10.1029/WR010i006p01199

González-Quirós, A., & Comte, J.-C. (2021). Hydrogeophysical model calibration and uncertainty analysis via full integration of PEST/PEST++ and COMSOL. *Environmental Modelling & Software*, *145*, 105183. https://doi.org/10.1016/j.envsoft.2021.105183

Graf, A., Klosterhalfen, A., Arriga, N., Bernhofer, C., Bogena, H., Bornet, F., & Vereecken, H. (2020). Altered energy partitioning across terrestrial ecosystems in the European drought year 2018. *Philosophical Transactions of the Royal Society B: Biological Sciences*, *375*, 20190524. https://doi.org/10.1098/rstb.2019.0524

Hinnell, A. C., Ferré, T. P., Vrugt, J. A., Huisman, J. A., Moysey, S., Rings, J., & Kowalsky, M. B. (2010). Improved extraction of hydrologic information from geophysical data through coupled hydrogeophysical inversion. *Water Resources Research*, *46*(4). https://doi.org/10.1029/2008WR007060

Huisman, J. A., Hubbard, S. S., Redman, J. D., & Annan, A. P. (2003). Measuring soil water content with ground penetrating radar. *Vadose Zone Journal*, *2*, 476–491. https://doi.org/10.2136/vzj2003.4760

Huisman, J. A., Rings, J., Vrugt, J. A., Sorg, J., & Vereecken, H. (2010). Hydraulic properties of a model dike from coupled Bayesian and multi-criteria hydrogeophysical inversion. *Journal of Hydrology*, *380*, 62–73. https://doi.org/10.1016/j.jhydrol.2009.10.023

Irving, J., & Singha, K. (2010). Stochastic inversion of tracer test and electrical geophysical data to estimate hydraulic conductivities. *Water Resources Research*, *46*(11). https://doi.org/10.1029/2009wr008340

IUSS Working Group WRB. (2007). *World reference base for soil resources* (World Soil Resources Reports No. 103). FAO.

Jadoon, K. Z., Weihermüller, L., Scharnagl, B., Kowalsky, M. B., Bechtold, M., Hubbard, S. S., & Lambot, S. (2012). Estimation of soil hydraulic parameters in the field by integrated hydrogeophysical inversion of time-lapse ground-penetrating radar data. *Vadose Zone Journal*, *11*(4), vzj2011.0177. https://doi.org/10.2136/vzj2011.0177

Jarvis, N., Larsbo, M., Lewan, E., & Garré, S. (2022). Improved descriptions of soil hydrology in crop models: The elephant in the room? *Agricultural Systems*, *202*, 103477. https://doi.org/10.1016/j.agsy.2022.103477

Jayawickreme, D. H., Van Dam, R. L., & Hyndman, D. W. (2010). Hydrological consequences of land-cover change: Quantifying the influence of plants on soil moisture with time-lapse electrical resistivity. *Geophysics*, *75*, WA43–WA50. https://doi.org/10.1190/1.3464760

Kemna, A., Vanderborght, J., Kulessa, B., & Vereecken, H. (2002). Imaging and characterisation of subsurface solute transport using electrical resistivity tomography (ERT) and equivalent transport models. *Journal of Hydrology*, *267*(3–4), 125–146. https://doi.org/10.1016/s0022-1694(02)00145-2

Kersebaum, K. C., Boote, K. J., Jorgenson, J. S., Nendel, C., Bindi, M., Frühauf, C., & Wegehenkel, M. (2015). Analysis and classification of data sets for calibration and validation of agro-ecosystem models. *Environmental Modelling & Software*, *72*, 402–417. https://doi.org/10.1016/j.envsoft.2015.05.009

Klotzsche, A., Jonard, F., Looms, M. C., van der Kruk, J., & Huisman, J. A. (2018). Measuring soil water content with ground penetrating radar: A decade of progress. *Vadose Zone Journal*, *17*, 180052. https://doi.org/10.2136/vzj2018.03.0052

Klotzsche, A., Lärm, L., Vanderborght, J., Cai, G., Morandage, S., Zörner, M., & Kruk, J. (2019). Monitoring soil water content using time-lapse horizontal borehole GPR data at the field-plot scale. *Vadose Zone Journal*, *18*, 190044. https://doi.org/10.2136/vzj2019.05.0044

Klotzsche, A., van der Kruk, J., He, G., & Vereecken, H. (2016). GPR full-waveform inversion of horizontal ZOP borehole data using GprMax. In *Proceedings of 2016 16th international conference of ground penetrating radar, GPR 2016* (pp. 1–5). Institute of Electrical and Electronics Engineers.

Koestel, J., Kemna, A., Javaux, M., Binley, A., & Vereecken, H. (2008). Quantitative imaging of solute transport in an unsaturated and undisturbed soil monolith with 3-D ERT and TDR. *Water Resources Research*, *44*(12). https://doi.org/10.1029/2007wr006755

Kool, J. B., Parker, J. C., & van Genuchten, M. Th. (1987). Parameter estimation for unsaturated flow and transport models—A review. *Journal of Hydrology*, *91*, 255–293. https://doi.org/10.1016/0022-1694(87)90207-1

Kravchenko, A. N., Toosi, E. R., Guber, A. K., Ostrom, N. E., Yu, J., Azeem, K., & Robertson, G. P. (2017). Hotspots of soil N_2O emission enhanced through water absorption by plant residue. *Nature Geoscience*, *10*, 496–500. https://doi.org/10.1038/ngeo2963

Kuhl, A. S., Kendall, A. D., Dam, R. L., & Hyndman, D. W. (2018). Quantifying soil water and root dynamics using a coupled hydrogeophysical inversion. *Vadose Zone Journal*, *17*, 170154. https://doi.org/10.2136/vzj2017.08.0154

Landl, M., Schnepf, A., Uteau, D., Peth, S., Athmann, M., Kautz, T., & Vanderborght, J. (2019). Modeling the impact of biopores on root growth and root water uptake. *Vadose Zone Journal*, *18*, 1–20. https://doi.org/10.2136/vzj2018.11.0196

Lärm, L., Bauer, F. M., Hermes, N., van der Kruk, J., Vereecken, H., Vanderborght, J., Nguyen, T. H., Lopez, G., Seidel, S. J., Ewert, F., Schnepf, A., & Klotzsche, A. (2023). Multi-year belowground data of minirhizotron facilities in Selhausen. *Scientific Data*, *10*(1), Article 672. https://doi.org/10.1038/s41597-023-02570-9

Lärm, L., Bauer, F. M., van der Kruk, J., Vanderborght, J., Morandage, S., Vereecken, H., & Klotzsche, A. (2024). Linking horizontal crosshole

GPR variability with root image information for maize crops. *Vadose Zone Journal*, 23(1), e20293. https://doi.org/10.1002/vzj2.20293

Looms, M. C., Binley, A., Jensen, K. H., Nielsen, L., & Hansen, T. M. (2008). Identifying unsaturated hydraulic parameters using an integrated data fusion approach on cross-borehole geophysical data. *Vadose Zone Journal*, 7, 238–248. https://doi.org/10.2136/vzj2007.0087

Looy, K. V., Bouma, J., Herbst, M., Koestel, J., Minasny, B., Mishra, U., & Vereecken, H. (2017). Pedotransfer functions in Earth system science: Challenges and perspectives. *Reviews of Geophysics*, 55, 1199–1256. https://doi.org/10.1002/2017rg000581

Lynch, J. P. (2007). Roots of the Second Green Revolution. *Australian Journal of Botany*, 55(5), 493–512. https://doi.org/10.1071/bt06118

Manoli, G., Rossi, M., Pasetto, D., Deiana, R., Ferraris, S., Cassiani, G., & Putti, M. (2015). An iterative particle filter approach for coupled hydro-geophysical inversion of a controlled infiltration experiment. *Journal of Computational Physics*, 283, 37–51. https://doi.org/10.1016/j.jcp.2014.11.035

Mboh, C. M., Huisman, J. A., & Vereecken, H. (2011). Feasibility of sequential and coupled inversion of time domain reflectometry data to infer soil hydraulic parameters under falling head infiltration. *Soil Science Society of America Journal*, 75, 775–786. https://doi.org/10.2136/sssaj2010.0285

Michot, D., Benderitter, Y., Dorigny, A., Nicoullaud, B., King, D., & Tabbagh, A. (2003). Spatial and temporal monitoring of soil water content with an irrigated corn crop cover using surface electrical resistivity tomography. *Water Resources Research*, 39(5). https://doi.org/10.1029/2002wr001581

Moghadas, D., Jadoon, K. Z., & McCabe, M. F. (2017). Spatiotemporal monitoring of soil water content profiles in an irrigated field using probabilistic inversion of time-lapse EMI data. *Advances in Water Resources*, 110, 238–248. https://doi.org/10.1016/j.advwatres.2017.10.019

Montzka, C., Herbst, M., Weihermüller, L., Verhoef, A., & Vereecken, H. (2017). A global data set of soil hydraulic properties and sub-grid variability of soil water retention and hydraulic conductivity curves. *Earth System Science Data*, 9, 529–543. https://doi.org/10.5194/essd-9-529-2017

Mualem, Y. (1976). A new model for predicting the hydraulic conductivity of unsaturated porous media. *Water Resources Research*, 12, 513–522. https://doi.org/10.1029/WR012i003p00513

Novák, V., & Hlaváčiková, H. (2018). *Applied soil hydrology*. Springer-Verlag GmbH. https://www.ebook.de/de/product/34760443/viliam_novak_hana_hlavacikova_applied_soil_hydrology.html. abgerufen.

Peters, A., Durner, W., & Wessolek, G. (2011). Consistent parameter constraints for soil hydraulic functions. *Advances in Water Resources*, 34, 1352–1365. https://doi.org/10.1016/j.advwatres.2011.07.006

Pleasants, M. S., dos A Neves, F., Parsekian, A. D., Befus, K. M., & Kelleners, T. J. (2022). Hydrogeophysical inversion of time-lapse ERT data to determine hillslope subsurface hydraulic properties. *Water Resources Research*, 58(4), e2021WR031073. https://doi.org/10.1029/2021wr031073

Pleasants, M. S., Kelleners, T. J., Parsekian, A. D., & Befus, K. M. (2023). A Comparison of Hydrological and Geophysical Calibration Data in Layered Hydrologic Models of Mountain Hillslopes. *Water Resources Research*, 59(2), e2022WR033506. https://doi.org/10.1029/2022wr033506

Poggio, L., Gimona, A., Brown, I., & Castellazzi, M. (2010). Soil available water capacity interpolation and spatial uncertainty modelling at multiple geographical extents. *Geoderma*, 160, 175–188. https://doi.org/10.1016/j.geoderma.2010.09.015

Pokorny, J. (2019). Evapotranspiration. In *Encyclopedia of ecology* (2nd ed., Vol. 2, pp. 292–303). https://doi.org/10.1016/b978-0-12-409548-9.11182-0

Priesack, E., & Durner, W. (2006). Closed-form expression for the multi-modal unsaturated conductivity function. *Vadose Zone Journal*, 5, 121–124. https://doi.org/10.2136/vzj2005.0066

Pütz, T., Kiese, R., Wollschläger, U., Groh, J., Rupp, H., Zacharias, S., & Vereecken, H. (2016). TERENO-SOILCan: A lysimeter-network in Germany observing soil processes and plant diversity influenced by climate change. *Environmental Earth Sciences*, 75, 1242. https://doi.org/10.1007/s12665-016-6031-5

Rahmati, M., Groh, J., Graf, A., Pütz, T., Vanderborght, J., & Vereecken, H. (2020). On the impact of increasing drought on the relationship between soil water content and evapotranspiration of a grassland. *Vadose Zone Journal*, 19, e20029. https://doi.org/10.1002/vzj2.20029

Richards, L. A. (1931). Capillary conduction of liquids through porous mediums. *Physics*, 1, 318–333. https://doi.org/10.1063/1.1745010

Roth, K., Schulin, R., Flühler, H., & Attinger, W. (1990). Calibration of time domain reflectometry for water content measurement using a composite dielectric approach. *Water Resources Research*, 26, 2267–2273.

Rucker, D. F., & Ferré, T. (2004). Parameter estimation for soil hydraulic properties using zero-offset borehole radar. *Soil Science Society of America Journal*, 68, 1560–1567. https://doi.org/10.2136/sssaj2004.1560

Samouëlian, A., Cousin, I., Tabbagh, A., Bruand, A., & Richard, G. (2005). Electrical resistivity survey in soil science: A review. *Soil and Tillage Research*, 83, 173–193. https://doi.org/10.1016/j.still.2004.10.004

Schnepf, A., Carminati, A., Ahmed, M. A., Ani, M., Benard, P., Bentz, J., & Vetterlein, D. (2022). Linking rhizosphere processes across scales: Opinion. *Plant and Soil*, 478, 5–42. https://doi.org/10.1007/s11104-022-05306-7

Sheets, K. R., & Hendrickx, J. M. (1995). Noninvasive soil water content measurement using electromagnetic induction. *Water Resources Research*, 31, 2401–2409. https://doi.org/10.1029/95wr01949

Simmer, C., Thiele-Eich, I., Masbou, M., Amelung, W., Bogena, H., Crewell, S., Diekkrüger, B., Ewert, F., Hendricks Franssen, H.-J., Huisman, J. A., Kemna, A., Klitzsch, N., Kollet, S., Langensiepen, M., Löhnert, U., Rahman, A. S. M. M., Rascher, U., Schneider, K., Schween, J., … Zerenner, T. (2015). Monitoring and modeling the terrestrial system from pores to catchments: The transregional collaborative research center on patterns in the soil–vegetation–atmosphere system. *Bulletin of the American Meteorological Society*, 96, 1765–1787. https://doi.org/10.1175/BAMS-D-13-00134.1

Šimůnek, J., van Genuchten, M. Th., & Šejna, M. (2013). *The HYDRUS-1D software package for simulating the one-dimensional movement of water, heat, and multiple solutes in variably-saturated media* (version 4.17). University of California-Riverside Research Reports.

Steelman, C. M., & Endres, A. L. (2011). Comparison of Petrophysical Relationships for Soil Moisture Estimation using GPR Ground Waves. *Vadose Zone Journal*, 10(1), 270–285. https://doi.org/10.2136/vzj2010.0040

Sugiura, N. (1978). Further analysis of the data by Akaike's information criterion and the finite corrections. *Communications in Statistics - Theory and Methods*, 7(1), 13–26. https://doi.org/10.1080/03610927808827599

Thorup-Kristensen, K., Cortasa, M. S., & Loges, R. (2009). Winter wheat roots grow twice as deep as spring wheat roots, is this important for N uptake and N leaching losses? *Plant and Soil*, *322*, 101–114. https://doi.org/10.1007/s11104-009-9898-z

Topp, G. C., Davis, J. L., & Annan, A. P. (1980). Electromagnetic determination of soil water content: Measurements in coaxial transmission lines. *Water Resources Research*, *16*, 574–582. https://doi.org/10.1029/wr016i003p00574

Tran, A. P., Dafflon, B., Hubbard, S. S., Kowalsky, M. B., Long, P., Tokunaga, T. K., & Williams, K. H. (2016). Quantifying shallow subsurface water and heat dynamics using coupled hydrological-thermal-geophysical inversion. *Hydrology and Earth System Sciences*, *20*, 3477–3491. https://doi.org/10.5194/hess-20-3477-2016

Vanderborght, J., Leitner, D., Schnepf, A., Couvreur, V., Vereecken, H., & Javaux, M. (2023). Combining root and soil hydraulics in macroscopic representations of root water uptake. *Vadose Zone Journal*, *23*, e20273. https://doi.org/10.1002/vzj2.20273

van Genuchten, M. Th. (1980). A closed-form equation for predicting the hydraulic conductivity of unsaturated soils. *Soil Science Society of America Journal*, *44*, 892–898. https://doi.org/10.2136/sssaj1980.03615995004400050002x

Van Keulen, H., & Seligman, N. G. (1987). *Simulation of water use, nitrogen nutrition and growth of a spring wheat crop*. Cambridge University Press. https://doi.org/10.1017/S0021859600081582

Vereecken, H., Amelung, W., Bauke, S. L., Bogena, H., Brüggemann, N., Montzka, C., & Zhang, Y. (2022). Soil hydrology in the Earth system. *Nature Reviews Earth & Environment*, *3*, 573–587. https://doi.org/10.1038/s43017-022-00324-6

Vereecken, H., Huisman, J. A., Bogena, H., Vanderborght, J., Vrugt, J. A., & Hopmans, J. W. (2008). On the value of soil moisture measurements in vadose zone hydrology: A review. *Water Resources Research*, *44*(4). https://doi.org/10.1029/2008wr006829

Vereecken, H., Schnepf, A., Hopmans, J. W., Javaux, M., Or, D., Roose, T., & Young, I. M. (2016). Modeling soil processes: Review, key challenges, and new perspectives. *Vadose Zone Journal*, *15*, vzj2015.09.0131. https://doi.org/10.2136/vzj2015.09.0131

Warren, C., Giannopoulos, A., & Giannakis, I. (2016). gprMax: Open source software to simulate electromagnetic wave propagation for ground penetrating radar. *Computer Physics Communications*, *209*, 163–170. https://doi.org/10.1016/j.cpc.2016.08.020

Weigand, M., Zimmermann, E., Michels, V., Huisman, J. A., & Kemna, A. (2022). Design and operation of a long-term monitoring system for spectral electrical impedance tomography (sEIT). *Geoscientific Instrumentation, Methods and Data Systems*, *11*(2), 413–433. https://doi.org/10.5194/gi-11-413-2022

Weihermüller, L., Huisman, J. A., Hermes, N., Pickel, S., & Vereecken, H. (2013). A new TDR multiplexing system for reliable electrical conductivity and soil water content measurements. *Vadose Zone Journal*, *12*, 1–11. https://doi.org/10.2136/vzj2012.0194

Weihermüller, L., Huisman, J. A., Lambot, S., Herbst, M., & Vereecken, H. (2007). Mapping the spatial variation of soil water content at the field scale with different ground penetrating radar techniques. *Journal of Hydrology*, *340*, 205–216. https://doi.org/10.1016/j.jhydrol.2007.04.013

Wesseling, J. G. (1991). *CAPSEV: Steady state moisture flow theory, program description, and user manual* (Report No. 37). Winand Staring Centre.

Yeh, T.-C. J., & Šimůnek, J. (2002). Stochastic fusion of information for characterizing and monitoring the vadose zone. *Vadose Zone Journal*, *1*, 207–221. https://doi.org/10.2136/vzj2002.2070

Yu, Y., Weihermüller, L., Klotzsche, A., Lärm, L., Vereecken, H., & Huisman, J. A. (2021). Sequential and coupled inversion of horizontal borehole ground penetrating radar data to estimate soil hydraulic properties at the field scale. *Journal of Hydrology*, *596*, 126010. https://doi.org/10.1016/j.jhydrol.2021.126010

Zhang, Y., Weihermüller, L., Toth, B., Noman, M., & Vereecken, H. (2022). Analyzing dual porosity in soil hydraulic properties using soil databases for pedotransfer function development. *Vadose Zone Journal*, *21*, e20227. https://doi.org/10.1002/vzj2.20227

How to cite this article: Lärm, L., Weihermüller, L., Rödder, J., van der Kruk, J., Vereecken, H., & Klotzsche, A. (2025). Spatial variability of hydraulic parameters of a cropped soil using horizontal crosshole ground penetrating radar. *Vadose Zone Journal*, *24*, e20389. https://doi.org/10.1002/vzj2.20389

APPENDIX
Appendix A: Synthetic one-dimensional field study—Different measurement intervals

TABLE A1   Results of the synthetic study.

		Lower boundary	Upper boundary	SHP Forward	GPR days	Daily
Plow layer	θ_r (cm^3 cm^{-3})	0	0.01	0.002	0.006	0.005
	θ_s (cm^3 cm^{-3})	0.2	0.3	0.25	0.25	0.251
	α (1 cm^{-1})	0.01	0.1	0.0795	0.0749	0.0763
	n (-)	1.1	1.3	1.118	1.122	1.122
	K_s (cm day^{-1})	180	200	199.57	190.54	192.06
	λ (-)	4	6	4.59	5.026	5.091

(Continues)

TABLE A1 (Continued)

		Lower boundary	Upper boundary	SHP Forward	GPR days	Daily
Subsoil layer	θ_r (cm^3 cm^{-3})	0	0.01	0.009	0.004	0.005
	θ_s (cm^3 cm^{-3})	0.35	0.4	0.387	0.388	0.384
	α (1 cm^{-1})	0.007	0.01	0.0086	0.0087	0.0085
	n (-)	1.1	1.4	1.358	1.351	1.352
	K_s (cm day^{-1})	140	180	159.52	159.73	162.52
	λ (-)	−1	0	−0.6	−0.625	−0.498
				R^2	1.0	0.9990

Note: Comparison of the SHP of the forward model and the synthetic sequential inversion runs. R^2 is the variation between the synthetic GPR-derived SWC values and the modeled SWC values.

Abbreviations: GPR, ground penetrating radar; SHP, soil hydraulic parameters.
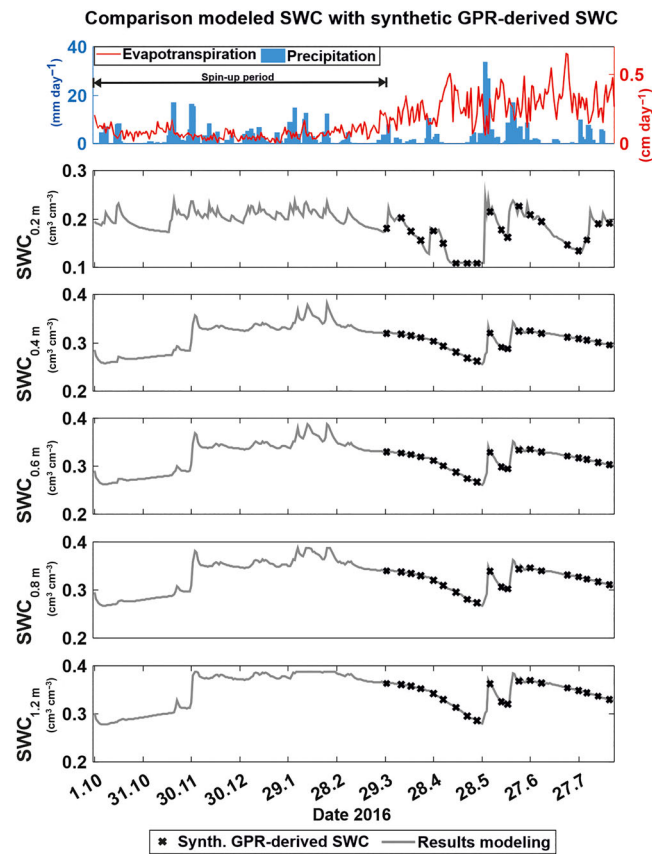

FIGURE A1 Results of the synthetic modeling. The black crosses indicate the synthetic GPR-SWC (ground penetrating radar-soil water content) values and the gray line represents the SWC optimized by the SCE-UA (Shuffled-Complex-Evolution algorithm).

Appendix B: Correlation between λ and K_S for the upscaling results
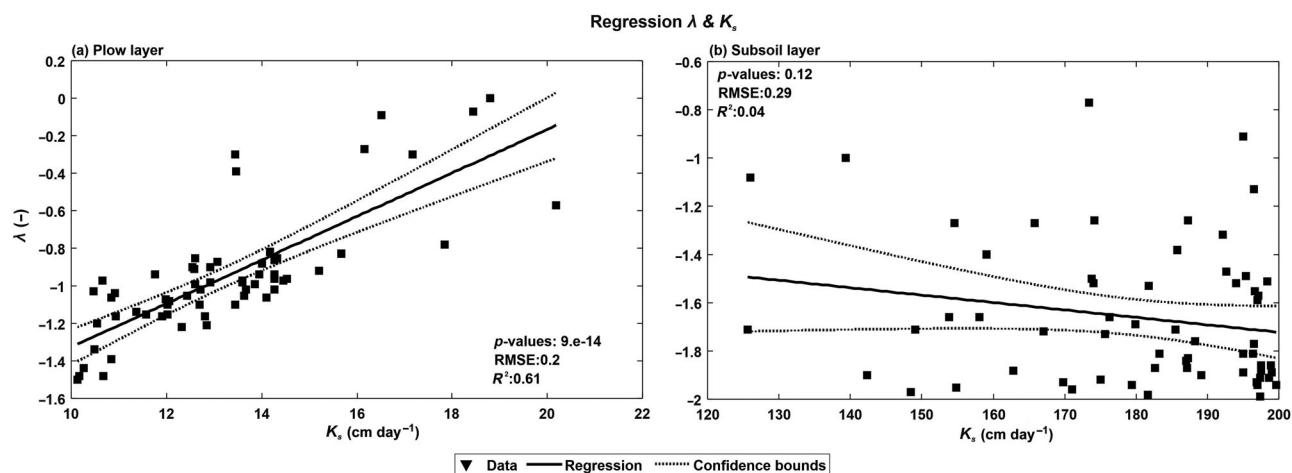

FIGURE B1 Correlation between λ and K_S for the semi-3D inversion results, for the plow layer (a) and subsoil layer (b), respectively.